

RESEARCH ARTICLE

10.1002/2015GB005359

Key Points:

- Decadal oceanic carbon sink is more variable than previously recognized
- Decadal variations mostly originate from extratropics
- The cumulative carbon uptake over 30 years is smaller than suggested by previous studies

Supporting Information:

- Supporting Information S1

Correspondence to:

P. Landschützer,
Peter.Landschuetzer@mpimet.mpg.de

Citation:

Landschützer, P., N. Gruber, and D. C. E. Bakker (2016), Decadal variations and trends of the global ocean carbon sink, *Global Biogeochem. Cycles*, 30, 1396–1417, doi:10.1002/2015GB005359.

Received 16 DEC 2015

Accepted 13 SEP 2016

Accepted article online 20 SEP 2016

Published online 5 OCT 2016

Decadal variations and trends of the global ocean carbon sink

Peter Landschützer^{1,2}, Nicolas Gruber¹, and Dorothee C. E. Bakker³
¹Institute of Biogeochemistry and Pollutant Dynamics, ETH Zürich, Zürich, Switzerland, ²Max Planck Institute for Meteorology, Hamburg, Germany, ³Centre for Ocean and Atmospheric Sciences, School of Environmental Sciences, University of East Anglia, Norwich, UK

Abstract We investigate the variations of the ocean CO₂ sink during the past three decades using global surface ocean maps of the partial pressure of CO₂ reconstructed from observations contained in the Surface Ocean CO₂ Atlas Version 2. To create these maps, we used the neural network-based data interpolation method of Landschützer et al. (2014) but extended the work in time from 1998 to 2011 to the period from 1982 through 2011. Our results suggest strong decadal variations in the global ocean carbon sink around a long-term increase that corresponds roughly to that expected from the rise in atmospheric CO₂. The sink is estimated to have weakened during the 1990s toward a minimum uptake of only -0.8 ± 0.5 Pg C yr⁻¹ in 2000 and thereafter to have strengthened considerably to rates of more than -2.0 ± 0.5 Pg C yr⁻¹. These decadal variations originate mostly from the extratropical oceans, while the tropical regions contribute primarily to interannual variations. Changes in sea surface temperature affecting the solubility of CO₂ explain part of these variations, particularly at subtropical latitudes. But most of the higher-latitude changes are attributed to modifications in the surface concentration of dissolved inorganic carbon and alkalinity, induced by decadal variations in atmospheric forcing, with patterns that are reminiscent of those of the Northern and Southern Annular Modes. These decadal variations lead to a substantially smaller cumulative anthropogenic CO₂ uptake of the ocean over the 1982 through 2011 period (reduction of 7.5 ± 5.5 Pg C) relative to that derived by the Global Carbon Budget.

1. Introduction

Recent model- and data-based estimates suggest that the global ocean currently removes every year, on average, roughly 25% of the the carbon dioxide (CO₂) emitted into the atmosphere as a result of anthropogenic activities, i.e., fossil fuel burning, cement production, and land use change [Mikaloff Fletcher et al., 2006; Khatiwala et al., 2013; Le Quéré et al., 2015a]. This fraction appears not to have changed significantly through time, as a data-based reconstruction of the ocean inventory of anthropogenic CO₂ suggests that it has removed roughly 30% of all anthropogenic CO₂ emitted since the beginning of the industrial revolution [Sabine et al., 2004]. Yet the temporal and spatial variability of this important greenhouse gas sink is not well constrained, particularly not when considering decadal timescales and longer [McKinley et al., 2011; Fay and McKinley, 2013; Wanninkhof et al., 2013; Lovenduski et al., 2015]. Quantifying these longer-term variations of the ocean carbon sink is important not only in order to accurately establish global budgets for the anthropogenic CO₂ [Le Quéré et al., 2015a] but also in order to better understand the vulnerability of the ocean carbon sink to future climate change [e.g. Matear and Hirst, 1999; Ciais et al., 2013].

Until recently, our knowledge regarding the variability of the oceanic sink for CO₂ on decadal timescales largely stemmed from atmospheric inverse models and hindcast simulations with ocean forward models, yet recent assessments [e.g. Lenton et al., 2013; Schuster et al., 2013; Wanninkhof et al., 2013; Ishii et al., 2014] have revealed large differences between these estimates. In general, ocean forward models simulate low levels of variability [Le Quéré et al., 2003; Lovenduski and Gruber, 2008; Sarmiento et al., 2010]. Their sink strength varies by only few tenths of a Pg C yr⁻¹ from one year to the next and shows little decadal variation around the expected long-term trend toward a stronger sink induced by the increase in atmospheric CO₂ [see, e.g., Le Quéré et al., 2015a]. Atmospheric inversions [Peylin et al., 2005, 2013] suggests stronger variability, but the pattern and timing is generally rather incongruent with that of the ocean models. Further, the confidence in these estimates is relatively low, owing to the “leakage” of information from the more variable land to the ocean [Peylin et al., 2005].

Observations of the sea surface partial pressure of CO₂ ($p\text{CO}_2$) have the potential to constrain the variations of the oceanic sink strength for CO₂. But despite a strong increase in the number of measurements taken globally [Pfeil *et al.*, 2013; Bakker *et al.*, 2014], these observations remain rather sparse in time and space, severely limiting their use for global-scale assessments without any form of interpolation. Thus, most surface ocean $p\text{CO}_2$ -based studies remain restricted to local to regional scales and very few were able to assess multidecadal timescales. Those analyses that exist suggest a substantial amount of interannual to decadal variability in sea surface $p\text{CO}_2$ [e.g., Feely *et al.*, 1999, 2006; Gruber *et al.*, 2002; Schuster and Watson, 2007; Watson *et al.*, 2009; Fay and McKinley, 2013; Fay *et al.*, 2014] indicating, like the atmospheric inversions, a more variable carbon sink than suggested by the ocean model-based assessments.

Many of the regional variations in the air-sea CO₂ fluxes have been linked to distinct modes of climate variability. The globally most prominent and best known mode of variability in the CO₂ flux, i.e., the El Niño–Southern Oscillation (ENSO) climate mode [Feely *et al.*, 1999; Le Quéré *et al.*, 2003; McKinley *et al.*, 2004a, 2004b; Feely *et al.*, 2006; Rödenbeck *et al.*, 2014; Landschützer *et al.*, 2014], alters the equatorial Pacific source of CO₂ by up to $\pm 0.5 \text{ Pg C yr}^{-1}$. But on decadal timescales, the Pacific sink appears to vary much less, although significant differences have been described between the eastern and western tropical Pacific [Takahashi *et al.*, 2003]. In the North Atlantic, many studies found substantial interannual to decadal variations in this important sink for atmospheric CO₂, linking them to changes in the North Atlantic Oscillation [Gruber *et al.*, 2002; Corbière *et al.*, 2007; Schuster and Watson, 2007; Thomas *et al.*, 2008; Schuster *et al.*, 2009; Ullman *et al.*, 2009; Metzl *et al.*, 2010; McKinley *et al.*, 2011; Landschützer *et al.*, 2013]. In the Southern Ocean, atmospheric data and ocean model simulations suggested that the southward shift and intensification of the westerly wind belt associated with a trend toward a more positive Southern Annular Mode weakened the Southern Ocean carbon uptake between the 1970s and the early 2000s [Le Quéré *et al.*, 2007; Lovenduski and Gruber, 2008; Lovenduski *et al.*, 2015]. More recently, Landschützer *et al.* [2015a] demonstrated that this weakening stopped around the turn of the century and that the sink strength since then rebounded back to levels expected based on the increase in atmospheric CO₂.

While these observations suggest a substantial amount of interannual to decadal variations within each of the ocean basins, several studies showed that trends in the air-sea $p\text{CO}_2$ difference, i.e., $\Delta p\text{CO}_2$, converge to zero when the analyses are extended to multiple decades and when they cover entire ocean basins [McKinley *et al.*, 2011; Fay and McKinley, 2013; Tjiputra *et al.*, 2014]. As this difference is the primary driver for the air-sea exchange of CO₂, this near zero trend implies that the ocean carbon sink remains relatively constant over these multidecadal timescales. But also, this conclusion is hampered by data sparsity.

One of the key needs in order to quantify longer-term variations of the ocean carbon sink is internally consistent observations spanning multiple decades. Recognizing such needs, the surface ocean CO₂ measurement community created the Surface Ocean CO₂ Atlas (SOCAT) [Bakker *et al.*, 2014], which, in its second release, contains roughly 10 million observations from 1968 to 2011, i.e., covering the essential time span to investigate decadal variations. However, the temporal and spatial heterogeneity of the available observations represents a major challenge. Only few places in the global ocean exist where the sea surface $p\text{CO}_2$ has been monitored for decades at the same location (e.g., the Tropical Atmosphere Ocean array [see Feely *et al.*, 1999, 2006] or the subtropical time series sites near Hawaii (Hawaii Ocean Time Series, HOT) and near Bermuda (Bermuda Atlantic Timeseries Study, BATS) [see Gruber *et al.*, 2002; Keeling *et al.*, 2004; Bates, 2007; Bates *et al.*, 2014]; hence, biome scale averages [e.g., Fay and McKinley, 2013] or interpolation methods [Rödenbeck *et al.*, 2015] are currently used to fill data gaps existing throughout the majority of the global ocean.

In recent years a series of such data interpolation-based estimates of the global ocean carbon sink have been developed [Sasse *et al.*, 2013; Landschützer *et al.*, 2014; Rödenbeck *et al.*, 2014; Zeng *et al.*, 2014; Jones *et al.*, 2015], using novel machine learning-based regression and mixed layer budget techniques (cf. Rödenbeck *et al.* [2015], for an overview). Yet, with the exception of the study by Rödenbeck *et al.* [2014], none of these studies addressed the decadal variations of the ocean carbon sink and its drivers on a global scale.

Here we extend the temporal coverage of one of the above methods [Landschützer *et al.*, 2014] by 16 years to the period 1982 through 2011. From these $p\text{CO}_2$ maps, we calculate the exchange of CO₂ between the atmosphere and the ocean using a bulk gas transfer formulation. The resulting air-sea flux maps are then used to investigate three decades of air-sea CO₂ flux variability. Using these $p\text{CO}_2$ data, we aim to identify the main drivers of the interannual to decadal variability. In a last step, we use our global flux estimates to calculate the residual land sink needed to close the global carbon budget.

2. Data and Methods

We employed the SOM-FFN (Self-Organizing Map-Feed-Forward Network) neural network method designed by Landschützer *et al.* [2013] and spatially extended by Landschützer *et al.* [2014] to map the sea surface $p\text{CO}_2$ from the Surface Ocean CO_2 Atlas version 2 (SOCATv2) [Bakker *et al.*, 2014]. Specifically, we used the gridded $p\text{CO}_2$ data product [Sabine *et al.*, 2013] and interpolated the observations onto a global $1^\circ \times 1^\circ$ grid and a monthly temporal resolution. We extended the method from the period 1998 through 2011 covered by Landschützer *et al.* [2014] to the period 1982 through 2011 to enable us to investigate 30 years of variations in the sea surface $p\text{CO}_2$ (run identifier ETH30yr [Landschützer *et al.*, 2015b]). Landschützer *et al.* [2015a] presented the data from this statistical model for the Southern Ocean south of 35°S . Here we show, analyze, and discuss the global data set.

The method is based on a two-step approach, where in a first step the global ocean is clustered into 16 biogeochemical provinces, based on common patterns in sea surface temperature (SST), sea surface salinity, mixed layer depth, and the $p\text{CO}_2$ climatology of Takahashi *et al.* [2009], using a self-organizing map neural network approach. By using nonnormalized data in this step, we implicitly give most weight to the $p\text{CO}_2$ climatology. This ensures that we create spatially and temporally dynamic provinces that largely follow the seasonal cycle of the $p\text{CO}_2$ climatology. In a second step, we reconstruct the nonlinear relationships between a second set of environmental drivers (SST, sea surface salinity, atmospheric dry air CO_2 mixing ratio ($x\text{CO}_2$), mixed-layer depth, and satellite chlorophyll) and the available surface ocean CO_2 observations from the SOCATv2 database for each of the provinces established in step 1 individually. These relationships are then used together with the environmental drivers to reconstruct the temporal evolution of $p\text{CO}_2$ globally (except for the Arctic basin and other enclosed basins).

The temporal extension required us to update and change some of the input data used in our previous global study [Landschützer *et al.*, 2014], as several of them are not available prior to 1998. Namely, (i) we used the monthly climatology of chlorophyll (www.globcolour.info) from 1998 to 2013 as a predictor field for each year before 1998, (ii) we used a climatological mixed-layer product [de Boyer Montegut *et al.*, 2004], and (iii) we used the monthly Hadley Center EN4 salinity product [Good *et al.*, 2013]. These substitutions led to small changes in our estimates after 1998 (see supporting information Text S5 for details), while permitting us to extend the interpolation to the 1980s and early 1990s.

The monthly $p\text{CO}_2$ fields were then smoothed using a three-dimensional averaging filter, smoothing the nearest neighbor domain ($3 \times 3 \times 3$ domain) in time and space. The smoothing does not influence the long-term mean estimate, the trend, or the interannual variability, but it ensures the filtering out of the high-frequency variability that occurs particularly in coastal regions and at frontal zones.

One source of concern when extending the data back to the 1980s and early 1990s is the substantially smaller amount of data available then to constrain the reconstructed surface ocean $p\text{CO}_2$ (see Figure S9). In order to test the impact of data availability upon the reconstructions, we conducted two SOM-FFN runs where we artificially thinned the data by subsampling at 5 year intervals, i.e., 5 years of data followed by 5 years without data. The results reveal a robust ability of the SOM-FFN method to reconstruct the oceanic $p\text{CO}_2$ field (supporting information Text S5 and Figure S9), with differences during the periods of missing training data not exceeding the uncertainties of the reconstruction from 1990 onward. Exceptions are the first and last years, where the removal of training data leads to larger deviations. This is a result of the method relying on the trend in atmospheric CO_2 to construct the long-term trend in surface ocean $p\text{CO}_2$. If several years of training data are withheld from the training at the beginning or the end, then the trend is ill constrained during these years, leading to larger errors. This indicates that the SOM-FFN method is not well suited to extrapolate in time but that this method is not sensitive to changes in data availability when interpolating data in space and time (e.g., when the carbon sink is further reconstructed with additional data from the SOCATv3 database [Bakker *et al.*, 2016]). This is also confirmed by the method not showing any signs of temporal dependency with regard to the distribution of its residuals (see below and Figures S1–S4.)

In a recent intercomparison study of different $p\text{CO}_2$ mapping methods [Rödenbeck *et al.*, 2015], our SOM-FFN method was shown to be very skilled in reproducing the observed variability, particularly on interannual scales, where it performed among the best two methods out of the 14 compared. But a striking difference is that our SOM-FFN method reconstructs significantly lower year-to-year variability in the data poor regions compared to the top performing method by Rödenbeck *et al.* [2014]. This potential underestimation of

variability is also seen in the comparison of the reconstructed $p\text{CO}_2$ data with the observations from the long time series in the subtropical gyres (Figures S5 and S6). The low variability in our method is likely linked to the regression nature of the method, i.e., its limitation to extrapolate signals that are manifested in the driver data. Very encouraging, though, is that when considering decadal timescales, a good agreement exists between not only these two methods but also among most others, [Landschützer *et al.*, 2015a; Rödenbeck *et al.*, 2015], giving us confidence that our SOM-FFN method results are well suited to investigate decadal variations.

As in all our previous studies [Landschützer *et al.*, 2013, 2014, 2015a], we use a standard bulk parameterization [Wanninkhof, 1992; Garbe *et al.*, 2014] to calculate the air-sea flux density of CO_2 ($\text{mol C m}^{-2} \text{ yr}^{-1}$) from the reconstructed sea surface $p\text{CO}_2$ maps, namely:

$$F_{\text{CO}_2} = k_w \cdot S_{\text{CO}_2} \cdot (1 - f_{\text{ice}}) \cdot (p\text{CO}_2 - p\text{CO}_2^{\text{atm}}), \quad (1)$$

where we define a positive flux when CO_2 is outgassed from the ocean and a negative flux when the ocean takes up CO_2 . The fluxes are scaled to the ice-free area of each pixel, using sea ice cover data (f_{ice}) from Rayner *et al.* [2003]. The symbol k_w refers to the gas transfer velocity of CO_2 , computed following the Wanninkhof [1992] parameterization that assumes a quadratic dependence of wind speed, with the latter taken from the wind data of Dee *et al.* [2011]. We adjusted the scaling factor in the original Wanninkhof parameterization to reach a global mean transfer velocity of 16 cm h^{-1} , to match the new radiocarbon-based constraints [Sweeney *et al.*, 2007; Müller *et al.*, 2008; Graven *et al.*, 2012; Wanninkhof *et al.*, 2013]. The solubility of CO_2 in seawater (S_{CO_2}) is taken from Weiss [1974]. We estimate the partial pressure of atmospheric CO_2 ($p\text{CO}_2^{\text{atm}}$) from the dry air mixing ratio $x\text{CO}_2$ of GLOBALVIEW-CO2 [2014], taking into account the water vapor correction according to Dickson *et al.* [2007].

From the monthly $\Delta p\text{CO}_2 = p\text{CO}_2 - p\text{CO}_2^{\text{atm}}$ maps, we calculate the leading empirical orthogonal functions (EOF), following Glover *et al.* [2011]. Before we conducted the EOF analysis, a few data adjustments were required. First, we coarsened our $p\text{CO}_2$ field from the original $1^\circ \times 1^\circ$ to $2^\circ \times 2^\circ$ by binning the data in order to reduce the computational power needed to analyze the covariance matrix. Second, at each grid point, we deseasonalized the time series using a 12 month running average filter and detrended the resulting time series by removing the slope of the linear trend line. This deseasonalization and detrending permits us in our EOF analyses to extract the main modes of variability on interannual to decadal timescales without these signals being masked by the seasonal cycle and the long-term trend.

Owing to the scarcity of observations and/or high variance, we were not able to estimate $p\text{CO}_2$ for the Arctic Ocean and for the coastal ocean areas within 1° of the coastline (based on bathymetry [ETOPO2x2, 2006]). Therefore, our global integrated fluxes need to be corrected for these missing regions in order to represent a “true” global ocean flux. For the Arctic, we add a constant uptake of $-0.12 \pm 0.06 \text{ Pg C yr}^{-1}$ [Schuster *et al.*, 2013], while we refrain from making a correction for the coastal ocean to avoid double accounting, because we lack an independent estimate that corresponds to the missing coastal areas only.

Furthermore, our surface $p\text{CO}_2$ based estimates reflect the contemporary net flux, which is the superposition of the air-sea fluxes of natural and anthropogenic CO_2 [Gruber *et al.*, 2009]. Globally integrated, we expect the natural CO_2 component to amount to a net outgassing flux of about $0.45 \text{ Pg C yr}^{-1}$ [Jacobson *et al.*, 2007], balancing the net input of carbon from rivers minus burial. Accepting this value, we can estimate the global uptake flux of anthropogenic CO_2 by adding this outgassing value to the globally integrated contemporary flux, where we include the uptake in the Arctic. We then calculate the residual land sink using fossil fuel [Boden *et al.*, 2015] and land use change [Houghton *et al.*, 2012] emission estimates and subtracting the atmospheric accumulation rate (Edward Dlugokencky and Pieter Tans, 2015, NOAA/Earth System Research Laboratory (ESRL) [www.esrl.noaa.gov/gmd/ccgg/trends/]) as well as our oceanic sink estimates.

To report the error on the grid level, we adopt the method by Landschützer *et al.* [2014] to estimate the uncertainty of the integrated flux by combining the error from (a) the gridding of the available observations, (b) the root-mean squared mismatch between the SOM-FFN estimates and the gridded observations, and (c) the uncertainty stemming from the chosen air-sea flux parametrization plus 3 additional commonly used air-sea flux parametrizations [Wanninkhof, 1992; Wanninkhof and McGillis, 1999; Nightingale *et al.*, 2000]

To estimate the uncertainties of our reconstructed air-sea CO_2 fluxes, we follow the approach of Landschützer *et al.* [2014] and propagate the uncertainties from the different components (gridding error, error derived from the method, and air-sea gas exchange formulation) to the final flux product. The uncertainties of the spatially

and temporally integrated fluxes are then computed by propagation from the grid-level uncertainties, taking into account the substantial spatial autocorrelation of the $p\text{CO}_2$ measurements. A substantial part of the basin or global-scale uncertainties stems from systematic errors, largely owing to the ill constrained parameterization for the gas transfer velocity k_w . While this error source needs to be considered in full when computing annual carbon budgets, it is of lesser concern when considering trends and variations in the oceanic fluxes, since these systematic errors are not expected to vary in time [Landschützer *et al.*, 2014].

3. Evaluation

In order to test the robustness of our results, we performed a series of tests comparing how well our estimates are able to reproduce observations from the SOCATv2 database as well as independent data that were not included in the development of the data product. In the supporting information we present a detailed assessment, whereas we summarize the main findings here.

The method is able to reconstruct the available observations with almost zero bias and a root-mean-square deviation of less than $20 \mu\text{atm}$, confirming the findings of our previous work [Landschützer *et al.*, 2013, 2014, 2015a]. This is true for the global ocean but also for each of the major ocean basins (Pacific Ocean, Atlantic Ocean, Indian Ocean, and Southern Ocean) (see Figure S1). Overall, we find no correlation between the number of observations and the magnitude of the error, i.e., the temporal heterogeneity of the data does not introduce a detectable systematic bias in our estimates. Additionally, we find no systematic bias in space but rather a random error distribution as shown in Figure S3. However, similar to Landschützer *et al.* [2014], the largest residuals are found in the high-latitude oceans and in the equatorial Pacific, i.e., those regions characterized by the highest level of variability [Landschützer *et al.*, 2014].

The comparison with independent observations, i.e., observations not used in the SOM-FFN training, reveals larger differences. Nevertheless, the mean difference between our SOM-FFN estimates and observations from the LDEOv2013 database [Takahashi *et al.*, 2014] that are not included in SOCATv2 stays globally within $\pm 3 \mu\text{atm}$. An exception are the first 5 years of the analysis, i.e., 1982 through 1986 (see supporting information Figure S2), where the fewest observations exist and the Indian Ocean from 2002 to 2006. Figure S2c, however, reveals that the latter is likely a result from the low number of observations collected there after the millennium. The comparison with observations from the time series stations in the subtropical North Atlantic (BATS and Hydrostation S [Gruber *et al.*, 2002; Bates, 2007, 2012]) and North Pacific (HOT [Dore *et al.*, 2009]), where observations have been collected continuously over the last decades, suggest that although our estimates show strong decadal variability, the SOM-FFN output still underestimates the full seasonal amplitude, the interannual variability, and trends identified from the stations (see Figures S5 and S6). For the comparison to the time series stations, we use the CO2SYS software developed by Lewis and Wallace [1998] and updated by van Heuven *et al.* [2011] to calculate the sea surface $p\text{CO}_2$ from the directly measured carbonate system parameters, i.e., DIC and Alk, using also the concurrently measured temperature, salinity, and nutrients as input. This introduces an additional uncertainty of up to $6 \mu\text{atm}$ [see Millero, 1995] (see supporting information Text S2). A large fraction of the trend mismatch at these time series stations can be attributed to the 1980s and early 1990s period, where the least amount of SOCATv2 observations exist.

In summary, even though our reconstructed fields of the surface ocean $p\text{CO}_2$ are uncertain to within a few μatm , it is encouraging that we do not find any systematic errors, neither in time nor in space. This gives us confidence that our trend estimates are a robust feature of the data, although uncertainties in the regions and times with few observations remain substantial.

4. Air-Sea CO_2 Flux Variations and Trends

4.1. Global and Basin-Scale Fluxes

Over the last three decades, our data-based reconstruction of the annual mean CO_2 flux integrated over the world's ocean (including the Arctic) exhibits strong decadal variations around a long-term trend that is consistent with expectations based on the growth of atmospheric CO_2 (Figure 1). To quantify the latter, we used results from a global ocean biogeochemical model (the National Center for Atmospheric Research (NCAR) Community Climate System Model [Graven *et al.*, 2012]), which we had run with climatological meteorological forcing while prescribing the observed history of atmospheric CO_2 as a boundary condition. We then linearly scaled these model results so that they match the ocean inversion results for the contemporary CO_2 flux for the year 2000, i.e., an ocean uptake of $-1.7 \pm 0.4 \text{ Pg C yr}^{-1}$ [Gruber *et al.*, 2009].

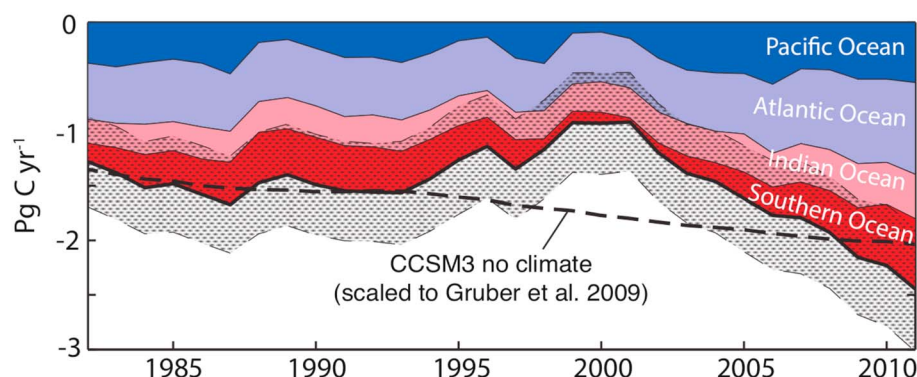


Figure 1. Time series of the annual mean and globally integrated air-sea CO_2 flux from 1982 to 2011 based on the SOM-FFN (run identifier ETH30yr) output (black thick line) and the contributions of each basin (separated at 44°S). The constant uptake flux of the Arctic Ocean [Schuster et al., 2013] is included in the Atlantic basin estimate. The hatched area indicates the uncertainty interval around the global mean. The dashed black line represents the expected uptake based on the increase in atmospheric CO_2 estimated from a hindcast simulation with an ocean biogeochemistry model (NCAR Community Climate System Model (CCSM) [Graven et al., 2012]) scaled to the global contemporary CO_2 flux estimated by Gruber et al. [2009].

The decadal variations are characterized by two distinct phases: Starting from a mean global uptake of about $-1.4 \pm 0.4 \text{ Pg C yr}^{-1}$ in the 1980s, the global ocean sink weakened throughout the 1990s to a minimum uptake of $-0.8 \pm 0.5 \text{ Pg C yr}^{-1}$ in 1999. Then the trend reversed, and since 2000, the global ocean sink has strengthened by more than 1 Pg C yr^{-1} to an uptake rate of $-2.3 \pm 0.6 \text{ Pg C yr}^{-1}$ in 2011. The uncertainties of our annual flux estimates are fairly large, leading to barely significant differences between individual years. But the decadal differences are clearly significant, as is the deviation from the long-term expected trend during the low uptake period from 1997 to 2002. The significance of the decadal fluctuation is furthered by the uncertainties of the decadal means and trends likely being smaller than those of any individual year. This is because of the systematic nature of a substantial fraction of the error in the global integral (e.g., gas transfer velocity), most of which no longer has to be considered when investigating longer-term trends [Landschützer et al., 2014].

The post 1999 strengthening trend was already identified in our earlier reconstruction [Landschützer et al., 2014] that covered only the period 1998 through 2011. Our extended 30 year reconstruction confirms this finding but suggests also a somewhat steeper trend for the post 1999 period, largely owing to the inclusion of new data. This period of a steeply increasing sink was also identified by Rödenbeck et al. [2014], albeit in their case masked by a much stronger level of interannual variability. Further support comes from several more independent reconstructions of the oceanic $p\text{CO}_2$ fields summarized by Rödenbeck et al. [2015], especially those that performed best against a data misfit-based metric.

Our extension back in time puts this recent strengthening of the oceanic sink into the longer temporal context, i.e., contrasting it with the relatively stagnant ocean carbon sink of the 1980s and the 1990 through 1999 period when the ocean carbon sink progressively weakened. This stagnant to weakening sink period is supported by the analyses of Fay and McKinley [2013], who identified $p\text{CO}_2$ trends in the ocean from 1990 to 2005 that were steeper than that in the atmosphere [see, e.g., Fay and McKinley, 2013, Figure 4]. A steeper trend results in a reduction of the air-sea gradient in $p\text{CO}_2$, i.e., a weaker sink. Also, reconstructions of Rödenbeck et al. [2014] indicate a weakening trend in the pre 1999 period. In summary and combining the pre- and post-1999 periods, our results suggest a substantially stronger decadal ocean carbon sink variability than expected based on previous, mainly model-based, estimates [see, e.g., Sarmiento et al., 2010; Le Quééré et al., 2015a, 2015b].

Figure 1 reveals that the decadal variations of the global ocean carbon uptake are not equally contributed to by the different ocean basins. The Southern Ocean uptake pattern follows that of the global ocean, with a reduction of the carbon sink in the 1990s and a reinvigoration since the turn of the millennium (see discussion by Landschützer et al. [2015a]). In fact, roughly 50% of the global sink increase after 2002 can be attributed to the area south of 35°S . The Atlantic Ocean shows a similar pattern with a decreasing uptake trend in the 1990s followed by an accelerated carbon uptake after 2000. In contrast, the Pacific Ocean as a whole contributes less to the decadal trends, although it dominates the variability on interannual timescales. The Indian Ocean

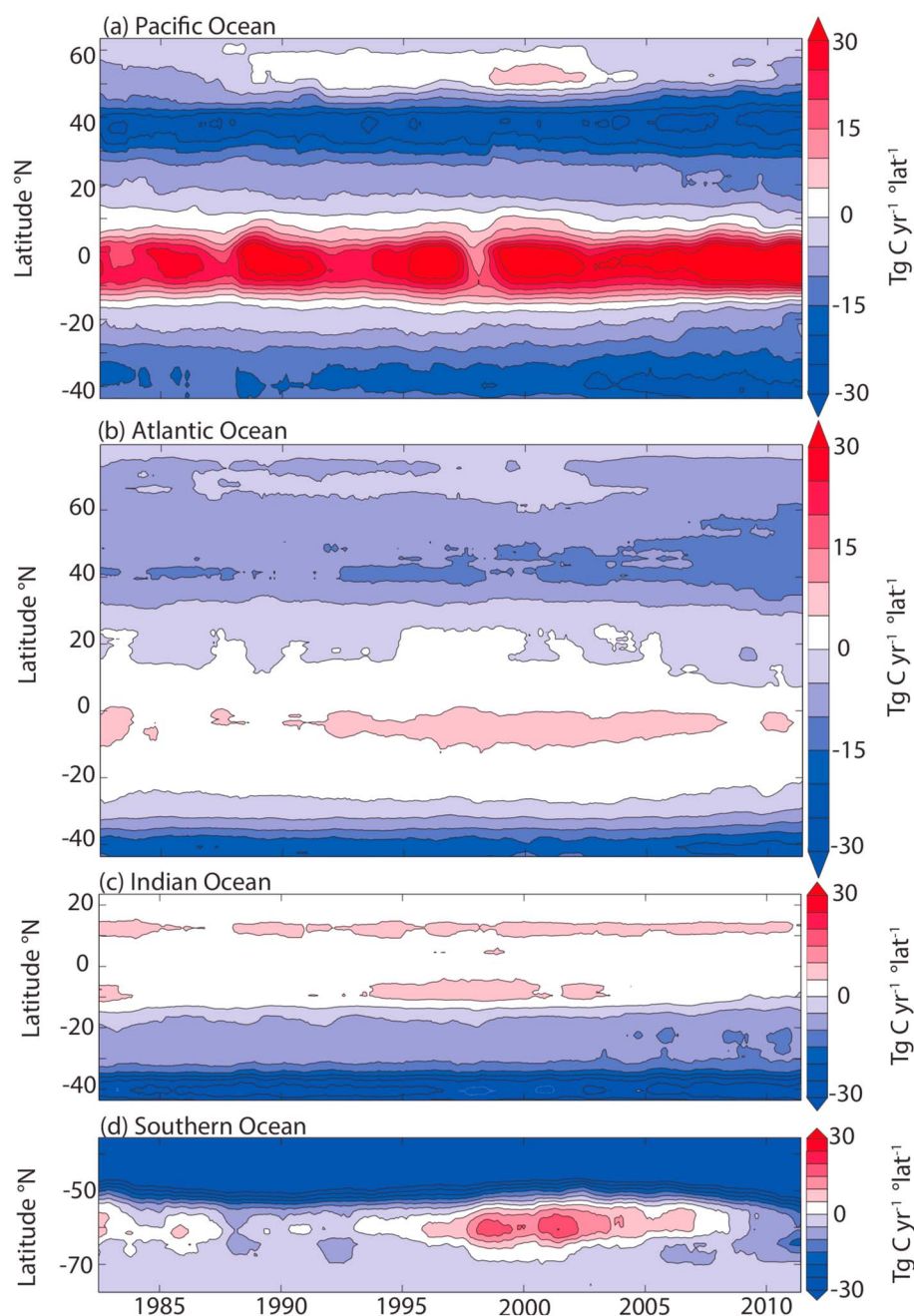


Figure 2. Hovmöller plots of the zonally integrated air-sea flux from 1982 to 2011 for (a) the Pacific Ocean, (b) the Atlantic Ocean, (c) the Indian Ocean, and (d) the Southern Ocean. While Figures 2a–2c are plotted for the basins north of 44°S, the northern boundary of the Southern Ocean was extended to 35°S to be comparable with the results by Landschützer *et al.* [2015a]). The time series were deseasonalized and smoothed using a 12 month moving average filter.

shows a fairly steady carbon uptake up to 1998, followed by a slight increase in the most recent decade. But this adds little to the global ocean flux increase of the last decade.

4.2. Zonal Mean Flux Variations

The separation of the basin-wide trends into zonal mean variations by means of Hovmöller diagrams reveals a distinct pattern within each basin (Figures 2 and 3). The latitudinal variations of the zonally integrated and deseasonalized air-sea CO₂ fluxes in each of the four major ocean basins in Figure 2 primarily depict the annual mean fluxes, dominated by tropical outgassing and CO₂ uptake in the temperate and high latitudes [Takahashi *et al.*, 2002, 2009; Gruber *et al.*, 2009; Landschützer *et al.*, 2014]. A closer inspection reveals substantial variations

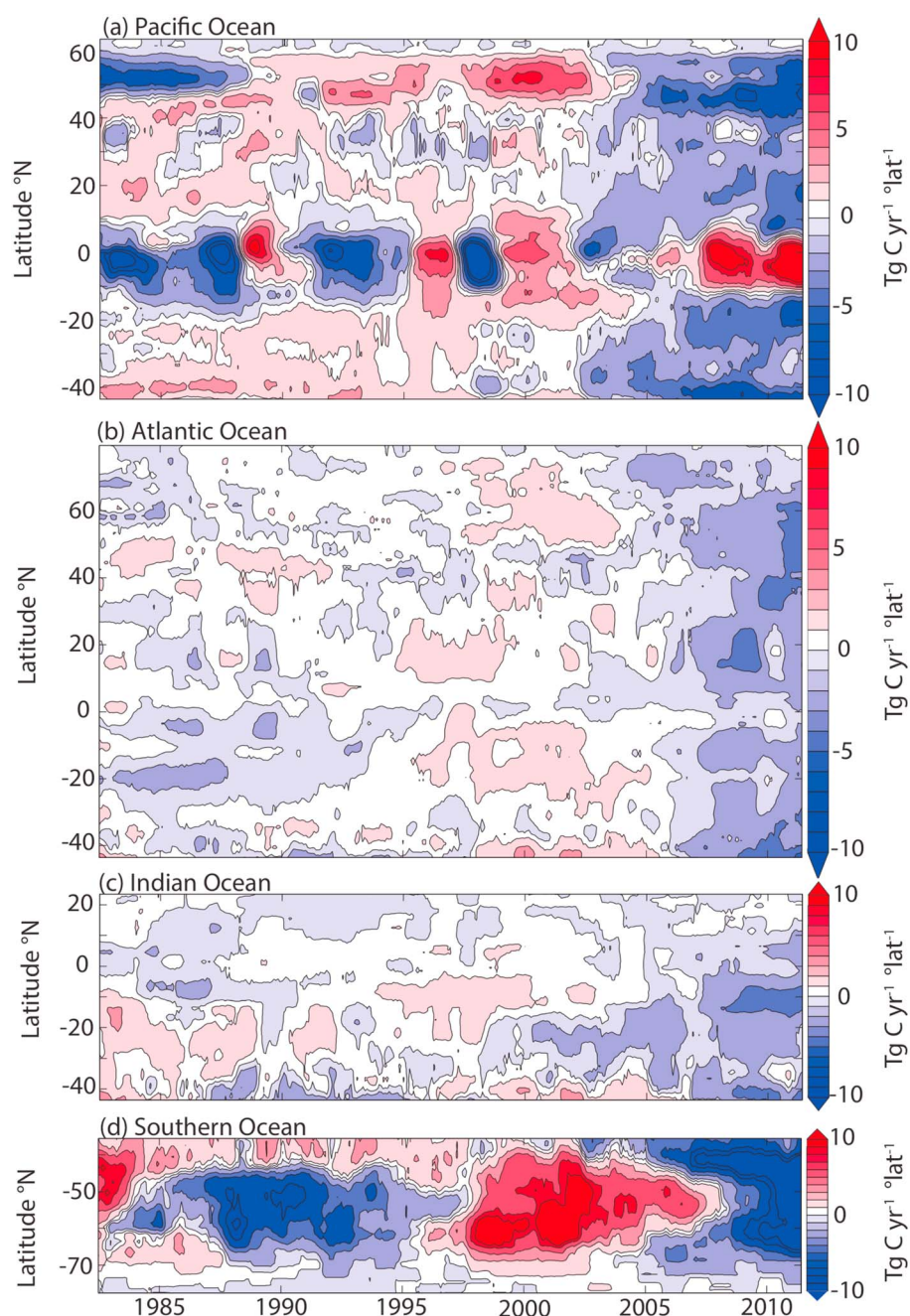


Figure 3. As Figure 2, except for the CO_2 flux anomalies. This anomaly time series was created by subtracting the 30 year mean flux and by smoothing the data using a 12 month moving average filter.

within each basin. These variations become more distinct by removing the long-term mean CO_2 flux and thus just plotting the anomalous component (Figure 3). Note that the different magnitude of the zonally integrated fluxes (Tg C yr^{-1} per degree latitude) is largely due to the differing longitudinal extent of each basin.

The Hovmöller diagram of the zonally integrated flux anomalies in the Pacific (Figure 3a) highlights the well-known ENSO driven variability within the equatorial Pacific [Feely *et al.*, 1999, 2006; Landschützer *et al.*, 2014; Rödenbeck *et al.*, 2014]. This pattern dominates the year-to-year variability. On longer, i.e., decadal timescales, two signals stand out. The first one is in the North Pacific between 50°N and 60°N and is characterized by an anomalous CO_2 sink in the 1980s, an anomalous source in the 1990s and early 2000s, and a return back to a strong sink by the late 2000s. The second signal that stands out in Figure 3a is characterized by an anomalous source over a substantial part of the Pacific in the late 1990s and then a nearly basin-wide

trend toward an anomalous sink starting around 2002. The almost basin-wide sink anomaly after 2002 is offset, however, by a strong anomalous outgassing in the equatorial band, explaining the absence of a strong decadal trend in the Pacific-wide integrated flux (Figure 1).

In contrast to the Pacific Ocean, the Atlantic Ocean (Figure 3b) has little variability in the equatorial region, though anomalies occur between the mid-1990s to the mid-2000s. But, as is the case for the Pacific, the Atlantic exhibits a whole basin tendency toward a stronger sink after 2000, following a period of an anomalous source that began around 1995. The Indian Ocean (Figure 3c) is reconstructed to vary the least of all basins, although it trends also toward a larger ocean CO₂ uptake during the last decade. As discussed by Landschützer *et al.* [2015a], the Southern Ocean (Figure 3d) experiences the strongest decadal variations and changes from negative anomalies (anomalous sink) in the late 1980s and early 1990s to strong positive anomalies (anomalous source) in the late 1990s and early 2000s followed by a negative anomaly after that, with most of the variability stemming from the region in the latitude band between 40°S and 65°S.

Contrasting the anomalous fluxes with their mean (Figure 3 versus Figure 2) reveals that in the post 2000 period, the strong sources have become stronger, and at the same time, the strong sinks have become stronger as well. Thus, the recent decade is characterized not only by a strengthening of the global ocean CO₂ uptake but also by a substantial intensification of the exchange of CO₂ between the ocean and atmosphere.

4.3. Spatiotemporal Pattern of the Air-Sea CO₂ Flux

In order to obtain more insight into the spatiotemporal pattern of the air-sea flux we separate it into a long-term trend component and into a suite of interannually to decadal varying components using an empirical orthogonal functions (EOFs) approach. We conduct the spatiotemporal separation on $\Delta p\text{CO}_2$, i.e., the difference between the surface ocean $p\text{CO}_2$ and that in the atmosphere, rather than the flux. This simplification aids us in our subsequent analyses of the drivers and is justified by nearly all of the reconstructed air-sea CO₂ flux variations being driven by variations in sea surface $p\text{CO}_2$. In contrast, changes in wind speed, temperature, and sea ice, i.e., those factors affecting the effective gas transfer coefficient ($k_w \cdot S_{\text{CO}_2} \cdot (1 - f_{\text{ice}})$) (equation (1)), contribute comparatively little (see supporting information Text S3). Given our focus on interannual to decadal variations, the analyses were performed with deseasonalized data.

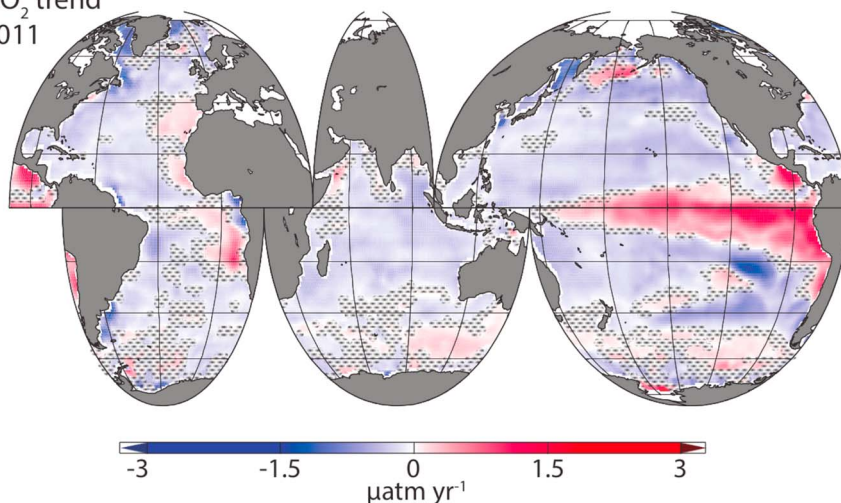
The global map of the long-term trend of $\Delta p\text{CO}_2$ (Figure 4a) depicts overall a relatively uniform negative pattern with the eastern equatorial Pacific cold tongue standing out with its strongly positive $\Delta p\text{CO}_2$ trend values. The global mean $\Delta p\text{CO}_2$ trend (ocean minus atmosphere) amounts to $-0.10 \pm 0.04 \mu\text{atm yr}^{-1}$, which is slightly weaker than the expected trend of about $-0.2 \mu\text{atm yr}^{-1}$ based on the growth in atmospheric CO₂, computed from the NCAR CCSM model [Graven *et al.*, 2012]. This compares well with the findings of Fay *et al.* [2014], who suggested that globally, the long-term trends in the surface ocean $p\text{CO}_2$ do not differ substantially from that in the atmosphere on multidecadal timescales, i.e., a $\Delta p\text{CO}_2$ trend of near zero. We attribute the positive $\Delta p\text{CO}_2$ trend in the eastern tropical Pacific to a small but significant trend in ENSO toward a more negative (La Niña) state over our analysis period. However, this trend is largely a consequence of our analysis starting during a strong El Niño year (1982) and ending during a relatively strong La Niña episode (2011).

The EOF-based spatiotemporal separation of the detrended $\Delta p\text{CO}_2$ (Figures 4b and 4c) reveals two dominant modes, which together explain 53% of the variance. The third EOF explains only 13% of the variance and is therefore not considered, nor are any of the remaining EOFs.

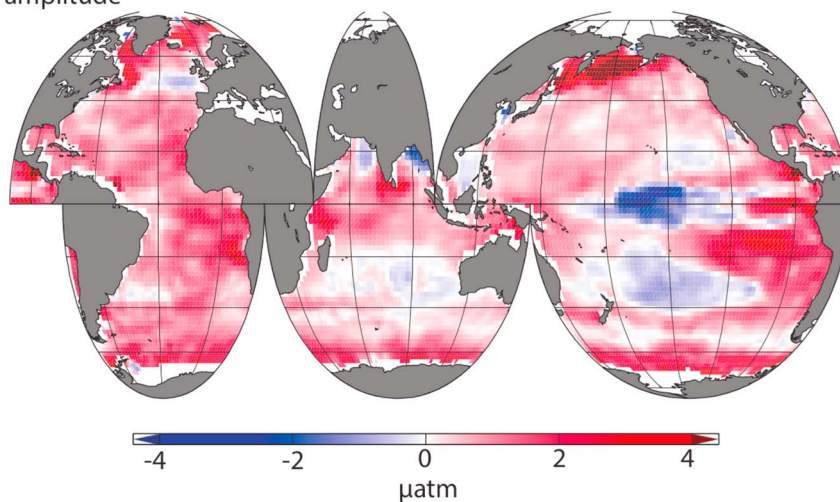
The spatial pattern of the leading EOF (EOF1) (Figure 4b) has nearly everywhere positive $\Delta p\text{CO}_2$ anomalies, with the exception of the central tropical Pacific, where substantial negative $\Delta p\text{CO}_2$ anomalies occur. This EOF is rather dominant, as it explains 34% of the variance. The strongest positive $\Delta p\text{CO}_2$ anomalies are found in the high northern latitudes of the Atlantic and Pacific, in the eastern tropical Pacific, and around the Antarctic continent. The associated time series of the first principal component (PC1) varies primarily on decadal timescales (Figure 5b). Starting from 1982, this principal component first increases, which when combined with the largely positive $\Delta p\text{CO}_2$ pattern implies a weakening ocean carbon sink. This trend ends in the late 1990s. Thereafter, the time series of the principal component of EOF1 decreases sharply to negative values, implying a steep increase of the oceanic sink for atmospheric CO₂. Thus, EOF1 appears to have picked up most of the decadal pattern of the global air-sea CO₂ flux seen in Figure 1.

EOF1 appears to be a decadal mode that is unique to the ocean carbon sink, as its time series does not correlate well with any of the major climate indices (see Table 1 and Figure 5). Concretely, we tested correlations with the multivariate ENSO index (MEI) [Wolter and Timlin, 2011], the Pacific Decadal Oscillation (PDO)

(a) $\Delta p\text{CO}_2$ trend
1982–2011



(b) EOF1 amplitude



(c) EOF2 amplitude

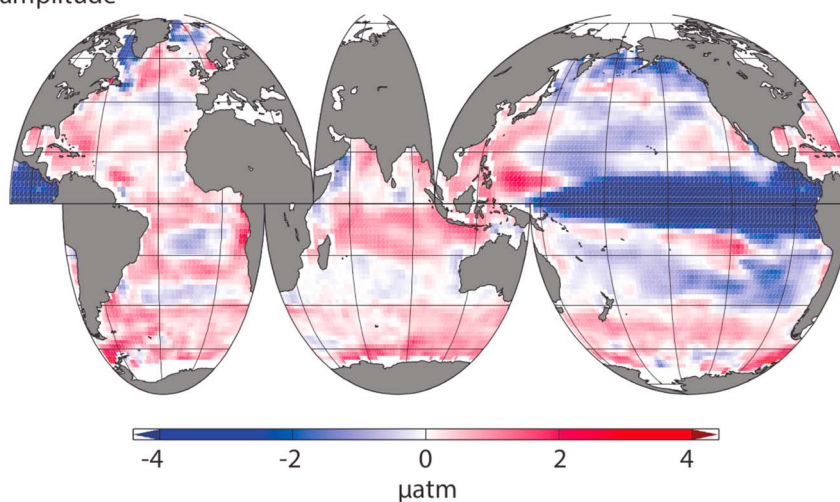


Figure 4. Maps of the different components contributing to variations and trends in the air-sea $p\text{CO}_2$ difference, i.e., $\Delta p\text{CO}_2 = p\text{CO}_2 - p\text{CO}_2^{\text{atm}}$. (a) Long-term linear trend ($\mu\text{atm yr}^{-1}$) of $\Delta p\text{CO}_2$, estimated by the slope of a least squares linear regression over the 1982 through 2011 period. (b) Spatial amplitude (μatm) of the first global empirical orthogonal function (EOF) of the detrended and deseasonalized $\Delta p\text{CO}_2$. This EOF explains 34% of the variance. (c) As in Figure 4b for the second EOF, which explains 19% of the variance.

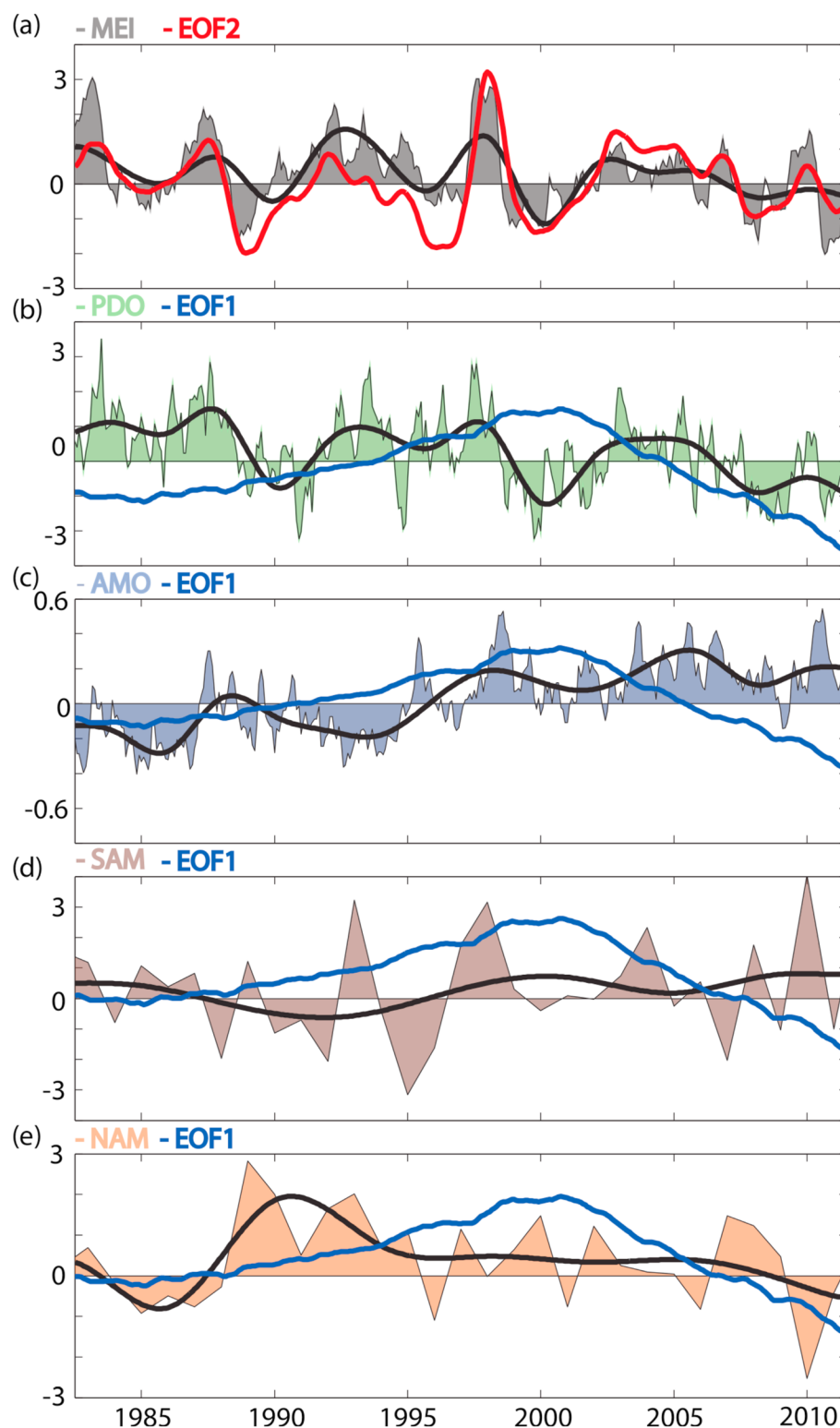


Figure 5. Time series of the principal components associated with EOF1 (blue) and EOF2 (red) of $\Delta p\text{CO}_2$, shown together with the time series of the major climate indices. MEI: Multivariate El Niño–Southern Oscillation Index, PDO: Pacific Decadal Oscillation, AMO: Atlantic Multidecadal Oscillation, SAM: Southern Annular Mode, NAM: Northern Annular Mode. For the SAM and NAM the winter indices are plotted here. Black lines illustrate a spline fit of the indices. The magnitude of the principal components is scaled to the indices for better visualization.

Table 1. Correlation Coefficients Between the First and Inverse Second EOF and the Main Climate Indices^a

	AMO	MEI	PDO	SAM	NAM
EOF1	0.14	0.07	0.01	−0.04	0.33
EOF2	0.12	0.62	0.48	0.09	−0.15

^aHigh-frequency variability has been removed by a smoothing spline fit. Bold numbers indicate significant correlations ($p \leq 0.05$).

[Zhang *et al.*, 1997], the Atlantic Multidecadal Oscillation (AMO) [Enfield *et al.*, 2001], the Northern Annular Mode or Arctic Oscillation (NAM or AO, December–March-based index) [Higgins *et al.*, 2002] and the Southern Annular Mode (SAM, winter index) [Marshall, 2003], which are available as dimensionless values. We were not separately considering the Interdecadal Pacific Oscillation (IPO) [e.g., England *et al.*, 2014], as its index is highly correlated to that of the PDO. We further used a smoothing spline fit to reduce the amount of high-frequency noise present in all indices.

In contrast to the decadal nature of the first EOF, the second EOF (EOF2) varies primarily on interannual timescales. It is quite a bit weaker than EOF1, explaining 19% of the total variance. The spatial pattern of EOF2 closely matches the typical ENSO pattern [see, e.g., Feely *et al.*, 2006] with a strong negative $\Delta p\text{CO}_2$ pattern in the tropical Pacific, creating periods of anomalously low outgassing during El Niño events, and exceptionally strong outgassing during La Niña events (Figure 4c). The connection of the second EOF with ENSO is further confirmed by the high correlation of the time series of the principal component of EOF2 (PC2) with the MEI ($R = 0.62$) (Table 1, see also Figure 5a). Owing to the high correlation between the MEI and the PDO, EOF2 also correlates significantly with the PDO index.

Viewed together, the EOF analyses demonstrates that more than 50% of the global air-sea CO_2 flux variability over the past 30 years can be described by the superposition of an ENSO-related interannual mode and with the center of action in the tropical Pacific, and a decadal mode, whose largest contribution comes from the high latitudes. It is also noteworthy that the relative contribution of the different modes of variability changed compared to the EOF analysis of our shorter reconstruction from 1998 to 2011 [Landschützer *et al.*, 2014]. During this shorter period, we found that interannual variations associated with ENSO dominated the global air-sea CO_2 flux variability, explaining 28% of the variance. Such a dominance had been suggested also by a number of modeling studies [e.g., McKinley *et al.*, 2004a]. However, our extended analysis shows that this is no longer the case when considering the last 30 years. Such a strong dominance of decadal timescale variability is not common for global ocean time series, as most of them tend to be dominated by ENSO-timescale variability or a multidecadal trend (e.g., sea surface temperature and sea level height). But the intense debate about the role of decadal variability in the ocean in connection with the period of reduced global warming [e.g., England *et al.*, 2014] illustrates the need to better understand the nature and source of such decadal timescale variations.

5. Drivers of the Interannual to Decadal Variations

In order to investigate the potential mechanisms driving the variations accompanied by the leading modes of variability in $\Delta p\text{CO}_2$, i.e., EOF1 and EOF2, we first split these two EOF modes into a temperature-driven (thermal) and into a nontemperature-driven (nonthermal) component:

$$\Delta p\text{CO}_2(x)_{\text{EOF}} = p\text{CO}_2(x)_{\text{EOF,thermal}} + \Delta p\text{CO}_2(x)_{\text{EOF,nonthermal}} \quad (2)$$

where x describes space. The nonthermal component includes the effect of changes in the surface ocean concentrations of dissolved inorganic carbon (DIC), alkalinity (Alk) and salinity. However, the direct effect of changes in salinity on surface ocean $p\text{CO}_2$ are of minor importance, so that the nonthermal component is primarily a result of changes in ocean circulation and/or biology affecting both DIC and Alk. Note that in our nonthermal trend, we implicitly exclude the effect of the long-term increase in DIC driven by the uptake of anthropogenic CO_2 . This is because of our choice to analyze trends in $\Delta p\text{CO}_2$, which results in the atmospheric $p\text{CO}_2$ trend being removed from the nonthermal component in surface ocean $p\text{CO}_2$. This choice is motivated by our desire to focus our analysis on the variations of the ocean carbon sink around the long-term trend driven by the change in atmospheric CO_2 .

We determine the thermal part by multiplying the temperature sensitivity of $p\text{CO}_2$ (taken from *Takahashi et al.* [1993]) with the EOF-associated SST signal $\text{SST}(x,t)_{\text{EOF}}$, determined by the slope of the regression of the observed sea surface temperature anomaly at each location on the time series of the principal component of the respective EOF. This gives:

$$p\text{CO}_2(x)_{\text{EOF,thermal}} = 0.0423 \cdot \langle p\text{CO}_2(x) \rangle \cdot \text{SST}(x)_{\text{EOF}} \quad (3)$$

where $\langle p\text{CO}_2(x) \rangle$ is the temporal mean in situ $p\text{CO}_2$. The nonthermal component is then computed from (2) by difference.

To connect these two components with possible underlying climatic drivers, we also regressed sea level pressure, wind velocity and wind stress, and the thermal and freshwater flux-driven buoyancy forcing on the time series of the principal components of the two EOFs. The data for these climatic drivers were taken from the ERA-Interim reanalysis [*Dee et al.*, 2011], with the buoyancy forcing computed from the heat and freshwater fluxes following *Cronin and Sprintall* [2009].

The separation of the two EOFs into their thermal and nonthermal components reveals for both EOFs a generally compensating nature between these two components (Figures 6a and 6b and 7a and 7b), reminiscent of their compensating nature on seasonal timescales [*Takahashi et al.*, 1993; *Sarmiento and Gruber*, 2006]. This compensating nature is primarily a result of the interaction between the temperature dependence of the CO_2 solubility and the temperature dependence of ocean density in the presence of ocean biology creating vertical gradients in DIC through the production and export of organic matter from the surface (see also discussion in *Sarmiento and Gruber* [2006]). On average, warming leads to a stronger stratification, which tends to lead to a more efficient biological pump, i.e., a larger fraction of the upward supplied DIC being fixed into organic matter and exported to depth. This leads to lower surface DIC concentrations, i.e., a smaller nonthermal component. Thus, while warming drives $p\text{CO}_2$ up (positive thermal component), circulation and biology (nonthermal component) drive $p\text{CO}_2$ down. The opposite tends to be the case when the surface ocean is being cooled. Despite this generally opposing tendency, there are distinct areas for both EOFs where one component dominates over the other one.

In the case of the ENSO-related second EOF, the strong positive thermal signal in the eastern equatorial Pacific associated with a positive (El Niño) phase (Figure 6a) is swamped by an even stronger negative anomaly from the nonthermal component (Figure 6b), leading to the overall negative $\Delta p\text{CO}_2$ signal in this region (Figure 4c). The negative nonthermal signal is the consequence of a near cessation of the upwelling of DIC-rich waters during El Niño events, which, in terms of its effect on $p\text{CO}_2$, dominates over the effect of the warming induced by the eastward propagating Kelvin wave (see discussion in, e.g., *Feely et al.* [1999]). The thermal signal outside the eastern tropical Pacific reflects primarily the SST regression pattern of ENSO [*Philander*, 1990], with cold anomalies in the North and South Pacific flanking the anomalously warm eastern Pacific and some alternating, but weak, warm, and cold teleconnection pattern in the Atlantic. But all of the thermal signals associated with the EOF2 mode outside the eastern and central equatorial Pacific are nearly perfectly compensated for by the nonthermal component, such that the only major signal left in the total signal, i.e., in $\Delta p\text{CO}_2$, is the nonthermally driven signal in the eastern equatorial Pacific.

The regressions of various climatic drivers on the time series of PC2 reveal the substantial sea level pressure and wind changes expected for a mode that is tightly connected to ENSO (Figures 6c–6f). During positive (El Niño) phases of EOF2, the low-pressure systems over the western tropical Pacific/eastern tropical Indian Ocean move eastward to the central tropical Pacific, leading to a sizeable decrease in the east-west pressure difference that normally characterizes the tropical Pacific. This induces strong westerly anomalies along the equator, particularly in the western Pacific causing a substantial reduction of the upwelling favorable trade winds. Figure 6c shows also the well-known extratropical atmospheric teleconnection pattern associated with ENSO, namely, the strengthening of the subpolar North Pacific Low [*Philander*, 1990]. The anomalous buoyancy forcing associated with positive (El Niño) phases of EOF2 leads to an increase in density along in the western equatorial Pacific due to reduced precipitation, but this effect is canceled by the decrease in density due to strong warming. But overall, these changes in buoyancy forcing are likely having a smaller effect on ocean circulation and mixing influencing DIC and Alk compared to the direct wind forcing influencing upwelling.

In the case of the decadal mode EOF1, the separation into its thermal and nonthermal components reveals that the globally nearly uniformly positive $\Delta p\text{CO}_2$ associated with this mode arises from a relatively patchy

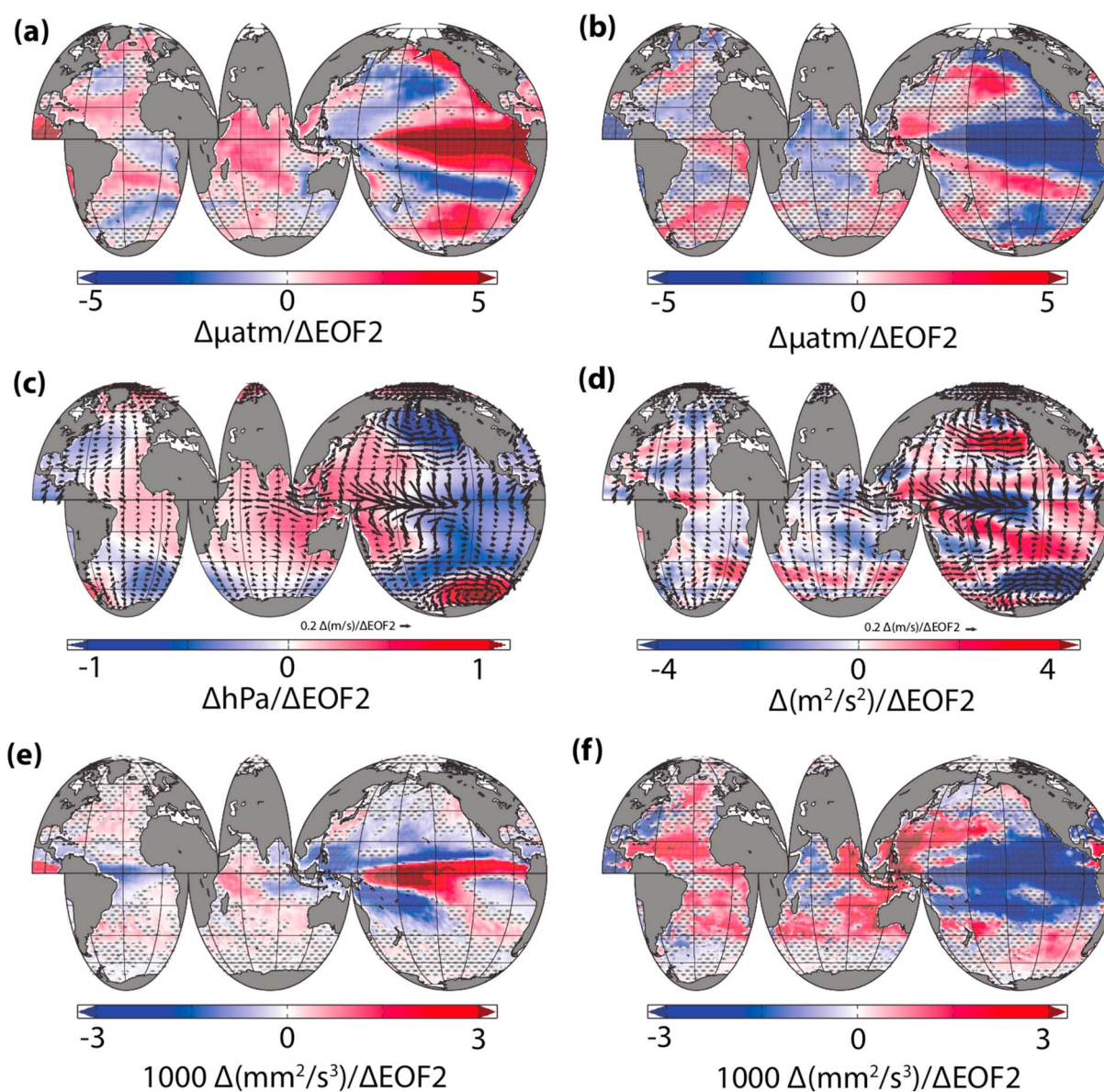


Figure 6. Global maps of the variations in $p\text{CO}_2$ components and potential drivers associated with the second empirical orthogonal function (EOF2) of the deseasonalized and detrended $\Delta p\text{CO}_2$. These maps were determined by regressing the quantity of interest on the time series of the principal component of EOF2 (PC2), i.e., they have units of the quantity of interest per unit change in PC2. (a) The thermal $p\text{CO}_2$ component, (b) the nonthermal $\Delta p\text{CO}_2$ component, (c) sea level pressure and wind vectors overlain as arrows, (d) the second moment of the wind with wind vectors, (e) the buoyancy freshwater flux, and (f) the buoyancy heat flux. Hatched areas indicate where the calculated regressions are not significantly different from zero ($p > 0.05$).

superposition of positive and negative regions in both components (Figures 7a and 7b). While the pattern looks rather random at first, a closer inspection reveals distinct and coherent patterns. To this end, we separately analyze the patterns in the northern and southern extratropics, respectively, and in the tropical belt.

Starting from the north, strong positive nonthermal anomalies characterize the subpolar gyres of both the Pacific and Atlantic (see also Figure 8), contrasting with (relatively weaker) negative anomalies covering much of the subtropical gyres. The thermal component not only has the opposite meridional pattern but also has the opposite relative strengths, i.e., weak (and largely non significant) negative anomalies in the subpolar gyres and strong positive anomalies in the subtropical gyres. Thus, the positive signal from the dominating nonthermal component in the subpolar gyres combines with the positive signal of the dominating thermal component in the subtropical gyres to create the observed relatively uniformly positive $\Delta p\text{CO}_2$ anomalies in the Northern Hemisphere extratropics during positive phases of EOF1.

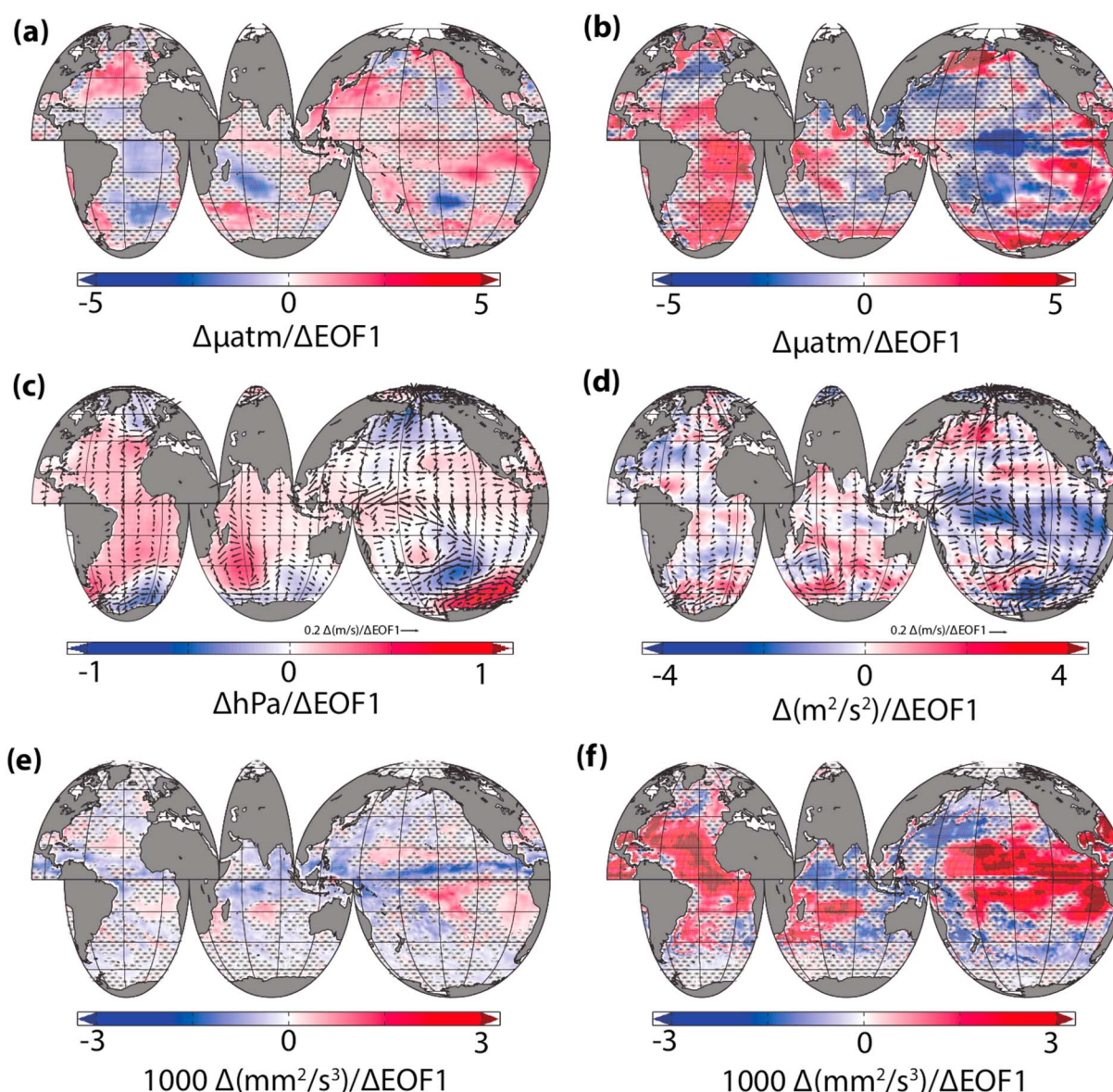


Figure 7. As Figure 6 but for the leading mode of variability (EOF1).

The potential climatic forcing driving this mode in the Northern Hemisphere extratropics becomes evident when inspecting the regressions of sea level pressure and wind speed on the time series of PC1 (Figure 8). These regressions reveal sea level pressure variabilities between the high-latitude low-pressure systems and the midlatitude/subtropical highs. During positive phases of this meridional mode, the pressure gradient becomes stronger, leading to stronger winds at about 40°N, causing also a substantially increased wind stress forcing onto the ocean (Figure 7d). In the subtropical latitudes, the winds and correspondingly also the wind stress become weaker. This meridional structure of the pressure and wind pattern has some reminiscence of the Arctic Oscillation or Northern Annular Mode (NAM) [Thompson and Wallace, 2000]. But relative to these modes, its center of low-pressure anomalies is shifted toward the Pacific. Also, the corresponding high-pressure anomalies are shifted to the south. Thus, while this mode has clear similarities to the NAM, it appears to be broader.

Viewed in the context of an annular mode, the pattern of the thermal component of EOF1 can be linked directly to the changes in wind, circulation, and heat fluxes (Figures 7c–7f) that drive a cooling at high latitudes and a warming at lower latitudes, analogous of the SST changes associated with positive phases of the NAM [Thompson and Wallace, 1998, 2000]. We interpret the nonthermal component to primarily reflect

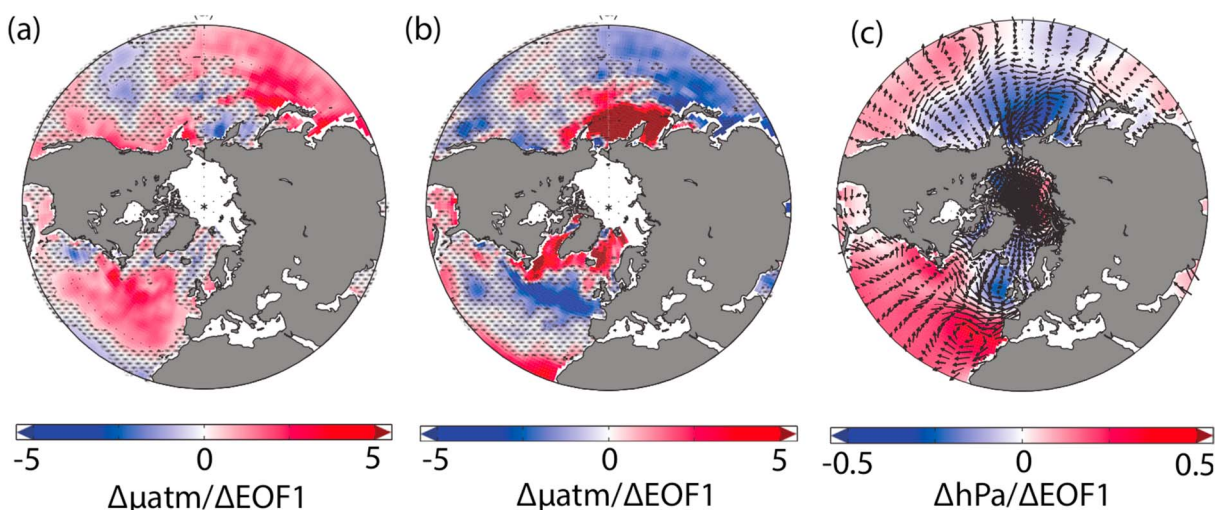


Figure 8. North polar stereographic projections of the $p\text{CO}_2$ components and potential drivers associated with the leading empirical orthogonal function (EOF1). (a) The thermal $p\text{CO}_2$ component, (b) the nonthermal $p\text{CO}_2$ component, and (c) sea level pressure and wind vectors overlain as arrows.

changes in upper ocean mixing. During positive phases of this mode, the colder SSTs and the stronger winds likely lead to deeper mixed layers in the subpolar gyres. This not only mixes up higher DIC concentrations to the surface but also tends to cause a stronger light limitation for phytoplankton. Both processes would cause the positive DIC anomalies that can explain the positive nonthermal $\Delta p\text{CO}_2$ anomalies. This may be enhanced through a stronger wind stress curl pumping more waters with elevated DIC up to the surface. The resulting positive nonthermal anomalies dominate over the cooling induced negative thermal component, explaining the overall positive $\Delta p\text{CO}_2$ signals in the subpolar gyres.

To the south, i.e., in the western temperate Pacific and in the eastern temperate Atlantic, the opposite appears to happen, with the warm SST anomalies shoaling the depth of the mixed layers, reducing the upward transport of DIC and stimulating phytoplankton growth. Again, this physical/biological signal may be enhanced through a more negative wind stress curl pumping more water down into the thermocline. Despite this possible enhancement, these nonthermal anomalies are weaker than the SST-driven thermal signals, leading to the overall positive $\Delta p\text{CO}_2$ anomalies in these temperate regions. Taken together, we have an ocean dynamics/biology controlled signal in the subpolar gyres and a SST-dominated signal in the temperate regions, explaining the overall synchronous behavior across the entire Northern Hemisphere. Such a meridional patterning, i.e., physics dominating the subpolar regions and temperature dominating the subtropics, has also been identified in several modeling studies, particularly for the North Atlantic [e.g. *Breeden and McKinley*, 2016; *Ullman et al.*, 2009; *Tjiputra et al.*, 2012] but also suggested by data-based analyses [e.g., *Gruber et al.*, 2002].

In the tropical Pacific, EOF1 appears to be connected to the decadal modifications of ENSO, i.e., it modifies the center of action between the eastern and the central Pacific, i.e., between the “classical” and the central (Modoki)-type El Niño [Ashok et al., 2007; Johnson, 2013] (Figure 5c). This effect is most strongly expressed in the nonthermal component (Figure 7b), where during positive phases of EOF1 the center of action of an El Niño is shifted westward to the central Pacific, causing even stronger negative nonthermal anomalies, likely stemming from even weaker upwelling. Conversely, positive nonthermal anomalies emerge in the far eastern tropical Pacific, likely due to somewhat stronger upwelling compared to a “normal,” eastern Pacific El Niño. This interpretation is consistent with the sea level pressure changes, the anomalous westerly winds, and the changes in precipitation (Figures 7c–7f). Concretely, when combining the spatial pattern of the EOF1 and EOF2 with their respective principal component time series, EOF1 made the 1997/1998 El Niño more central and the 1982/1983 El Niño more eastern.

In the Southern Hemisphere extratropics, the spatial patterns of the two components of EOF1 have some similarity to those in the Northern Hemisphere extratropics, particularly for the nonthermal component. Positive anomalies in the nonthermal component in the very high southern latitudes are flanked in the north by negative anomalies of this component. These regions also tend to be warmer, leading to positive

anomalies in the thermal component. An exception is the South Atlantic, which is characterized by a strong positive nonthermal component and a somewhat weaker negative thermal component.

Much of these pattern of change by the two components were already described and discussed by *Landschützer et al.* [2015a]. They pointed out that the weakening period of the Southern Ocean carbon sink during the 1980s and 1990s was caused by a zonally symmetric climatic forcing pattern that was closely associated with a trend toward more positive phases of the Southern Annular Mode, i.e., a southward shift and intensification of the winds over the Southern Ocean. The associated increase in the upwelling of waters with high DIC caused a strong positive trend in the nonthermal component that was only weakly compensated for by a cooling induced negative trend in the thermal component (see also studies by, e.g., *Le Quéré et al.* [2007], *Lenton and Matear* [2007], *Lovenduski and Gruber* [2008]). In contrast, *Landschützer et al.* [2015a] showed that the reinvigoration period of the years post-2000 were characterized by a zonally more asymmetric forcing with distinct differences between the Atlantic and Pacific, whereby the thermal component dominated in the Pacific and the nonthermal in the Atlantic. With EOF1 attempting to capture the variations over the entire period with a spatially stationary pattern, such changes in the spatial distribution of the controlling mechanisms are not fully captured. Given the substantially longer period, we suspect that EOF1 has picked up most of its spatial signal in the Southern Hemisphere extratropics from the stagnant/weakening sink phase in the 1980s and 1990s, i.e., the period where the positive nonthermal component can be clearly linked to the changes in wind.

In summary, the decadal mode EOF1 appears to be driven primarily by climate variations that show some resemblance to the Northern and Southern Annular Mode pattern. Overall, these extratropical processes in the Northern and Southern Hemisphere appear to have acted in relative synchronicity over the last 30 years, leading globally to a relatively coherent mode. The correlation with the indices for the Northern and Southern Annular Modes are nevertheless low. We interpret this to be caused by at least two reasons: First, EOF1 may attempt to fit both the NAM and SAM pattern simultaneously, resulting in its peak to be in-between that of the SAM and NAM. Second, this could be furthered by the occurrence of the 1997/1998 El Niño, which happened to be primarily a central El Niño, pushing the time series of EOF1 toward a peak in the late 1990s. But with the annular modes capturing only a relative small fraction of the overall climate variability in the extratropics, it is very conceivable that the climate variations driving the variations in the global ocean carbon sink are clearly distinct from the SAM and NAM.

While we provided some hypotheses about the mechanisms driving the stalling and subsequent weakening of the global ocean carbon sink during the 1980s and 1990s and its subsequent strong increase, the true causes of these decadal variations have yet to be determined. Our interpretations remain limited because of the correlative nature of our arguments, since the data available to us do not permit us to differentiate between cause and effect nor do they allow us to firmly quantify them. Further, with 30 years of data, the time series is relatively short to fully assess decadal variations. Despite these limitations, our results provide a strong target for future studies using models and observations.

A particularly striking observation is the analogy between our reconstructed variations of the global ocean carbon sink over the last 30 years and the evolution of the global mean surface air temperature. Following a period of relatively rapid warming in the 1990s, the global mean rate of increase in surface air temperature slowed down considerably after 2000. This strongly reduced warming period, often (but not really correctly) referred to as a “hiatus” period, has been attributed to many potential causes, but changes in ocean circulation and ocean heat uptake appear to be the leading explanations [e.g., *Higgins*, 2013]. Of particular relevance for the global ocean carbon sink is the changes in the trade winds [*England et al.*, 2014] and the coalescence of decadal trends in the North Pacific with those in the North Atlantic [*Steinman et al.*, 2015]. *Steinman et al.* [2015] showed through a statistical analysis of global-scale SST pattern, that before 2000, the decadal modes of the Pacific and the Atlantic trended in different directions, while thereafter, the Pacific mode (related to the PDO/IPO) became strongly negative, while the Atlantic mode (related to the AMO) remained relatively constant, causing a nearly worldwide pattern of slower warming. It is thus conceivable, while also being speculative, that also some of the decadal shifts in the ocean carbon uptake can be attributed to these changes in the Earth’s major decadal climate modes.

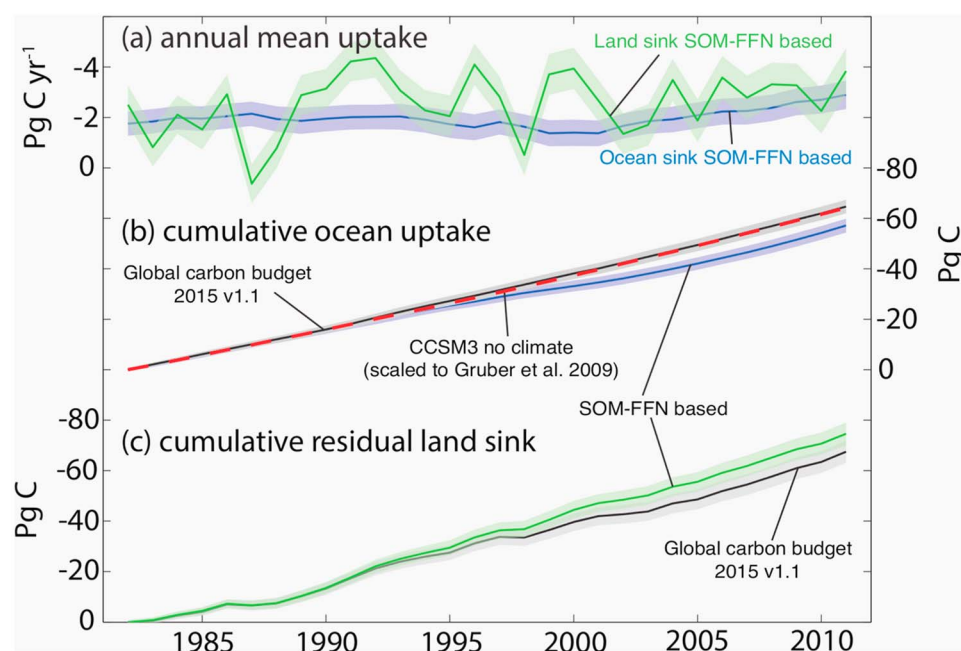


Figure 9. The evolution of the global anthropogenic carbon budget from 1982 through 2011. (a) Annual mean ocean sink for anthropogenic CO_2 based on the results of this study (blue) and the residual land carbon sink (green) calculated by the difference between the emissions of fossil fuel and cement CO_2 , ocean uptake, atmospheric accumulation and land use change. (b) Cumulative anthropogenic carbon uptake by the ocean estimated from the global carbon budget by the Global Carbon Project [Le Quéré *et al.*, 2015a] (black), this study (blue) and the expected uptake by the ocean based on the increase of atmospheric CO_2 alone (no climate) from the CCSM3 ocean model [Graven *et al.*, 2012], scaled to the long-term mean anthropogenic CO_2 uptake estimated by Gruber *et al.* [2009] (red). The shaded area illustrates the cumulative uncertainty of the neural network estimate (SOM-FFN) and the uncertainty from the global carbon budget [Le Quéré *et al.*, 2015a], calculated from the square-root of the squared sum of the annual mean uncertainties. (c) Cumulative residual land sink from the global carbon budget (black) and this study (green). The shaded area illustrates the uncertainty interval based on the neural network estimate and the uncertainty from the global carbon budget [Le Quéré *et al.*, 2015a], calculated from the square-root of the squared sum of the annual mean uncertainties. Negative values indicate carbon sinks.

6. Implications for the Global Carbon Budget

The next question is how the strong decadal variations in the ocean uptake affects our understanding of the global carbon cycle and of the global anthropogenic carbon budget, as put together on a yearly basis by the Global Carbon Project (GCP) [Le Quéré *et al.*, 2015a]. This is particularly relevant since in most of these budgets, the oceanic uptake variability is derived from ocean models [Sarmiento *et al.*, 2010; Le Quéré *et al.*, 2015a] that are known to underestimate the variability in the surface ocean fluxes [Landschützer *et al.*, 2014; Rödenbeck *et al.*, 2015].

Figure 9a compares the annual mean ocean uptake of anthropogenic CO_2 derived from this study (net flux plus river outgassing) to the implied residual land sink calculated as the difference between fossil fuel emissions, land use change, the ocean carbon sink, and the atmospheric accumulation rate. In contrast to the ocean carbon sink, the residual land sink varies little on decadal timescales but does so greatly from year to year, with a magnitude exceeding $\pm 3 \text{ Pg C yr}^{-1}$.

The difference between our new $p\text{CO}_2$ -based estimate of the ocean carbon sink and the previous estimates from the Global Carbon Budget becomes evident when comparing the cumulative oceanic carbon uptake (Figure 9b). The shaded area illustrates the cumulative uncertainty of our SOM-FFN estimate. The figure shows that the cumulative ocean carbon sink in the GCP budget (Global Carbon Budget 2015 v1.1) largely follows the expected increase due to atmospheric CO_2 , whereas the strong decadal variations of our estimate leads through time to a substantial deviation from this trend line. After 30 years, the GCP budget suggests a cumulative uptake of $64.6 \pm 2.7 \text{ Pg C}$, while our estimate is $57.1 \pm 2.8 \text{ Pg C}$, i.e., $7.5 \pm 5.5 \text{ Pg C}$ less carbon uptake by the ocean. As a consequence, this leads to an additional $\sim 7.5 \pm 8.8 \text{ Pg C}$ cumulative uptake by the land biosphere

from 1982 to 2011, implying a $0.25 \text{ Pg C yr}^{-1}$ stronger land sink, on average, compared to the GCP based estimate (Figure 9c). However, given the high uncertainty of the observation-based method in combination with the uncertainties from all other components, this land sink difference is not significant.

7. Summary and Conclusions

We expanded the method developed by Landschützer *et al.* [2013] and Landschützer *et al.* [2014] to reconstruct the surface ocean $p\text{CO}_2$ over three decades from 1982 to the end of 2011. We use high-frequency winds and a standard quadratic bulk formulation [Wanninkhof, 1992], scaled to a more recent gas transfer estimate [Wanninkhof *et al.*, 2013], to calculate monthly maps of the air-sea flux of CO_2 between the ocean and the atmosphere. The resulting air-sea flux reveals strong variability, particularly on interannual timescales in the tropical Pacific and on decadal timescales in the extratropical regions. This indicates that the global ocean carbon sink is strongly influenced by natural variability, with a stalling of the global ocean carbon sink in the 1980s, a reduction in the 1990s, and a strong increase in the ocean carbon sink since the turn of the millennium.

We find that these changes are well captured by the leading mode of variability of the air-sea $p\text{CO}_2$ difference, $\Delta p\text{CO}_2$, which we link primarily to major reorganizations of the extratropical weather patterns, which have some similarity to the Southern and Northern Annular Modes. The decadal up and down of the global ocean carbon sink is strikingly analogous to the decadal changes in ocean heat uptake driving variations in the rate of growth of surface air temperature. Furthermore, we find that on interannual timescales, the equatorial Pacific is playing a major role regarding the air-sea flux variability, manifested in the second largest mode of variability (EOF2) globally.

While our reconstructions of the ocean carbon sink variability over the last 30 years represent a major step forward in our understanding of the ocean carbon sink, there remain substantial uncertainties. One area needing attention is the level of interannual variability in the global carbon sink, especially the difference in the reconstructions by Rödenbeck *et al.* [2014] and this method. A second area is the better and more quantitative elucidation of the mechanisms driving the ocean carbon sink variations. The third area is to develop data-based methods to distinguish forced trends from internal ones, i.e., to develop methods to attribute the changes to whether they emerge as a result of anthropogenic climate change or natural (internal) climate variability [e.g., McKinley *et al.*, 2016].

Despite the uncertainties, our results clearly indicate that climate variations have a strong impact on the global ocean carbon sink, an effect not fully captured by the current generation of ocean carbon cycle models. It is therefore essential to continue the observational efforts to reduce the uncertainties attached to the estimates and better determine the impact of natural variability on the global carbon budget. A better understanding of the processes that drive the ocean carbon sink variability will further benefit the assessment of the future ocean sink in the presence of climate change. Our results suggest that the ocean carbon sink could be more sensitive to shifts in weather and climate pattern than previously recognized, particularly on decadal timescales. This also suggests that future changes in climate have the potential to substantially alter the strength of the ocean carbon sink, with major implications for, e.g., the magnitude of the emissions consistent with the internationally agreed 2°C climate change target.

References

- Ashok, K., S. K. Behera, S. A. Rao, H. Weng, and T. Yamagata (2007), El Niño Modoki and its possible teleconnection, *J. Geophys. Res.*, *112*, C11007, doi:10.1029/2006JC003798.
- Bakker, D. C. E., et al. (2014), An update to the Surface Ocean CO_2 Atlas (SOCAT version 2), *Earth Syst. Sci. Data*, *6*(1), 69–90, doi:10.5194/essd-6-69-2014.
- Bakker, D. C. E., et al. (2016), A multi-decade record of high-quality $f\text{CO}_2$ data in version 3 of the Surface Ocean CO_2 Atlas (SOCAT), *Earth Syst. Sci. Data*, *8*, 383–413, doi:10.5194/essd-8-383-2016.
- Bates, N., Y. Astor, M. Church, K. Currie, J. Dore, M. González-Dávila, L. Lorenzoni, F. Muller-Karger, J. Olafsson, and M. Santa-Casiano (2014), A time-series view of changing ocean chemistry due to ocean uptake of anthropogenic CO_2 and ocean acidification, *27*, 1, 126–141, doi:10.5670/oceanog.2014.16.
- Bates, N. R. (2007), Interannual variability of the oceanic CO_2 sink in the subtropical gyre of the North Atlantic Ocean over the last 2 decades, *J. Geophys. Res.*, *112*, C09013, doi:10.1029/2006JC003759.
- Bates, N. R. (2012), Multi-decadal uptake of carbon dioxide into subtropical mode water of the North Atlantic Ocean, *Biogeosciences*, *9*, 2649–2659, doi:10.5194/bg-9-2649-2012.
- Boden, T., G. Marland, and R. Andres (2015), *Global, regional, and national fossil-fuel CO_2 emissions*, Carbon Dioxide Information Analysis Center, Oak Ridge Natl. Lab., U.S. Dept. of Energy, Oak Ridge, Tenn., doi:10.3334/CDIAC/00001_V2015.

Acknowledgments

Support for P. Landschützer, N. Gruber, and D.C.E. Bakker was provided by EU FP7 grant 264879 (CARBOCHANGE). P.L. and N.G. acknowledge additional support by the EU FP7 grant 283080 (GEO-CARBON) and ETH Zürich. The Surface Ocean CO_2 Atlas (SOCAT) is an international effort, supported by the International Ocean Carbon Coordination Project (IOCCP), the Surface Ocean Lower Atmosphere Study (SOLAS), and the Integrated Marine Biogeochemistry and Ecosystem Research program (IMBER), to deliver a uniformly quality-controlled surface ocean CO_2 database. The many researchers and funding agencies responsible for the collection of data and quality control are thanked for their contributions to SOCAT. Furthermore, we would like to thank G.A. McKinley and a second anonymous reviewer for their very constructive suggestions that helped us to improve the manuscript.

- Breeden, M. L., and G. A. McKinley (2016), Climate impacts on multidecadal $p\text{CO}_2$ variability in the North Atlantic: 1948–2009, *Biogeosciences*, **13**, 3387–3396, doi:10.5194/bg-13-3387-2016.
- Ciais, P., et al. (2013), *Climate Change 2013: The Physical Science Basis. Contribution of Working Group I to the Fifth Assessment Report of the Intergovernmental Panel on Climate Change*, chap. Carbon and Other Biogeochemical Cycles, Cambridge University Press, Cambridge, U. K., and New York.
- Corbière, A., N. Metzl, G. Reverdin, C. Brunet, and T. Takahashi (2007), Interannual and decadal variability of the oceanic carbon sink in the North Atlantic subpolar gyre, *Tellus*, **59B**, 168–178.
- Cronin, M. F., and J. Sprintall (2009), Wind-and buoyancy-forced upper ocean, in *Elements of Physical Oceanography: A derivative of the Encyclopedia of Ocean Sciences*, edited by S. A. Thorpe, pp. 237–245, Elsevier, Academic Press, London.
- de Boyer Montegut, C., G. Madec, A. S. Fischer, A. Lazar, and D. Iudicone (2004), Mixed layer depth over the global ocean: An examination of profile data and a profile-based climatology, *J. Geophys. Res.*, **109**, C12003, doi:10.1029/2004JC002378.
- Dee, D. P., S. M. Uppala, A. J. Simmons, P. Berrisford, P. Poli, S. Kobayashi, U. Andrae, U. A. Balsamada, G. Balsamo, and P. Bauer (2011), The ERA-Interim reanalysis: Configuration and performance of the data assimilation system, *Q. J. R. Meteorol. Soc.*, **137**(656), 553–597, doi:10.1002/qj.828.
- Dickson, A. G., C. L. Sabine, and J. R. Christian (Eds.) (2007), *Guide to Best Practices for Ocean CO_2 Measurements*, PICES Special Publication, IOCCP Report No. 8, Sidney, Canada.
- Dore, J. E., R. Lukas, D. W. Sadler, D. M. Church, and M. J. Karl (2009), Physical and biogeochemical modulation of ocean acidification in the central North Pacific, *Proc. Natl. Acad. Sci. U.S.A.*, **106**, 12235–12240.
- Enfield, D. B., A. M. Mestas-Nunez, and P. J. Trimble (2001), The Atlantic multidecadal oscillation and its relation to rainfall and river flows in the continental U.S., *Geophys. Res. Lett.*, **28**, 2077–2080.
- England, M. H., S. McGregor, P. Spence, G. A. Meehl, A. Timmermann, W. Cai, A. S. Gupta, M. J. McPhaden, A. Purich, and A. Santoso (2014), Recent intensification of wind-driven circulation in the Pacific and the ongoing warming hiatus, *Nat. Clim. Change*, **4**(3), 222–227.
- ETOPO2x2 (2006), 2-minute gridded global relief data (ETOPO2v2), *Tech. Rep.*, U.S. Department of Commerce, National Oceanic and Atmospheric Administration, National Geophysical Data Center, Boulder, Colo.
- Fay, A. R., and G. A. McKinley (2013), Global trends in surface ocean $p\text{CO}_2$ from in situ data, *Global Biogeochem. Cycles*, **27**, 541–557, doi:10.1002/gbc.20051.
- Fay, A. R., G. A. McKinley, and N. S. Lovenduski (2014), Southern Ocean carbon trends: Sensitivity to methods, *Geophys. Res. Lett.*, **41**, 6833–6840, doi:10.1002/2014GL061324.
- Feely, R. A., R. Wanninkhof, T. Takahashi, and P. Tans (1999), Influence of El Niño on the equatorial Pacific contribution to atmospheric CO_2 accumulation, *Nature*, **398**, 597–601, doi:10.1038/19273.
- Feely, R. A., T. Takahashi, R. Wanninkhof, M. J. McPhaden, C. E. Cosca, S. C. Sutherland, and M.-E. Carr (2006), Decadal variability of the air-sea CO_2 fluxes in the equatorial Pacific Ocean, *J. Geophys. Res.*, **111**, C08S90, doi:10.1029/2005JC003129.
- Garbe, C. S., et al. (2014), *Ocean-Atmosphere Interactions of Gases and Particles*, pp. 55–112, chap. Transfer Across the Air-Sea Interface, Springer, Berlin.
- GLOBALVIEW- CO_2 (2014), *Cooperative Atmospheric Data Integration Project—Carbon Dioxide*, CD-ROM, NOAA ESRL, Boulder, Colo. [Also available on Internet via anonymous FTP to ftp.cmdl.noaa.gov, Path: ccg/co2/GLOBALVIEW.]
- Glover, D. M., W. J. Jenkins, and S. C. Doney (2011), *Modelling Methods for Marine Science*, Cambridge University Press, Cambridge, U. K., and New York.
- Good, S. A., M. J. Martin, and N. A. Rayner (2013), EN4: Quality controlled ocean temperature and salinity profiles and monthly objective analyses with uncertainty estimates, *J. Geophys. Res. Oceans*, **118**, 6704–6716, doi:10.1002/2013JC009067.
- Graven, H. D., N. Gruber, R. Key, S. Khaliwala, and X. Giraud (2012), Changing controls on oceanic radiocarbon: New insights on shallow-to-deep ocean exchange and anthropogenic CO_2 uptake, *J. Geophys. Res.*, **117**, C10005, doi:10.1029/2012JC008074.
- Gruber, N., C. D. Keeling, and N. R. Bates (2002), Interannual variability in the North Atlantic Ocean carbon sink, *Science*, **298**, 2374–2378, doi:10.1126/science.1077077.
- Gruber, N., et al. (2009), Oceanic sources, sinks, and transport of atmospheric CO_2 , *Global Biogeochem. Cycles*, **23**, GB1005, doi:10.1029/2008GB003349.
- Higgins, I. M. (2013), The cause of the pause, *Nature*, **501**, 318–319.
- Higgins, R. W., A. Leetmaa, and V. E. Kousky (2002), Relationships between climate variability and winter temperature extremes in the United States, *J. Clim.*, **15**, 1555–1572.
- Houghton, R., G. van der Werf, R. DeFries, M. Hansen, J. House, C. Le Quéré, J. Pongratz, and N. Ramankutty (2012), Carbon emissions from land use and land-cover change, *Biogeosciences*, **9**, 5125–5142, doi:10.5194/bg-9-5125-2012.
- Ishii, M., et al. (2014), Air-sea CO_2 flux in the Pacific Ocean for the period 1990–2009, *Biogeosciences*, **11**, 709–734.
- Jacobson, A. R., S. E. Mikaloff Fletcher, N. Gruber, J. Sarmiento, and M. Gloor (2007), A joint atmosphere-ocean inversion for surface fluxes of carbon dioxide: 2. Regional results, *Global Biogeochem. Cycles*, **21**, GB1020, doi:10.1029/2006GB002703.
- Johnson, N. C. (2013), How many ENSO flavors can we distinguish?, *J. Clim.*, **26**(13), 4816–4827, doi:10.1175/JCLI-D-12-00649.1.
- Jones, S. D., C. Le Quéré, C. Rödenbeck, A. C. Manning, and A. Olsen (2015), A statistical gap-filling method to interpolate global monthly surface ocean carbon dioxide data, *J. Adv. Model. Earth Syst.*, **7**, 1554–1575, doi:10.1002/2014MS000416.
- Keeling, C. D., H. Brix, and N. Gruber (2004), Seasonal and long-term dynamics of the upper ocean carbon cycle at station ALOHA near Hawaii, *Global Biogeochem. Cycles*, **18**, GB4006, doi:10.1029/2004GB002227.
- Khaliwala, S., T. Tanhua, S. Mikaloff Fletcher, M. Gerber, S. C. Doney, H. D. Graven, N. Gruber, G. A. McKinley, A. Murata, A. F. Rios, and C. L. Sabine (2013), Global ocean storage of anthropogenic carbon, *Biogeosciences*, **10**, 2169–2191, doi:10.5194/bg-10-2169-2013.
- Landschützer, P., N. Gruber, D. C. E. Bakker, U. Schuster, S. Nakaoka, M. R. Payne, T. Sasse, and J. Zeng (2013), A neural network-based estimate of the seasonal to inter-annual variability of the Atlantic Ocean carbon sink, *Biogeosciences*, **10**, 7793–7815, doi:10.5194/bg-10-7793-2013.
- Landschützer, P., N. Gruber, D. C. E. Bakker, and U. Schuster (2014), Recent variability of the global ocean carbon sink, *Global Biogeochem. Cycles*, **28**, 927–949, doi:10.1002/2014GB004853.
- Landschützer, P., et al. (2015a), The reinvigoration of the Southern Ocean carbon sink, *Science*, **349**, 1221–1224, doi:10.1126/science.aab2620.
- Landschützer, P., N. Gruber, and D. C. E. Bakker (2015b), A 30 years observation-based global monthly gridded sea surface $p\text{CO}_2$ product from 1982 through 2011, Carbon Dioxide Information Analysis Center, Oak Ridge National Laboratory, U.S. Department of Energy, Oak Ridge, Tenn., doi:10.3334/CDIAC/OTG.SPCO2_1982_2011_ETH_SOM-FFN.
- Le Quéré, C., et al. (2003), Two decades of ocean CO_2 sink and variability, *Tellus B*, **55**, 649–656, doi:10.1034/j.1600-0889.2003.00043.x.

- Le Quéré, C., et al. (2007), Saturation of the Southern Ocean CO₂ sink due to recent climate change, *Science*, *316*, 1735–1738, doi:10.1126/science.1136188.
- Le Quéré, C., et al. (2015a), Global carbon budget 2015, *Earth Syst. Sci. Data*, *7*(2), 349–396, doi:10.5194/essd-7-349-2015.
- Le Quéré, C., et al. (2015b), Global carbon budget 2014, *Earth Syst. Sci. Data*, *7*(1), 47–85, doi:10.5194/essd-7-47-2015.
- Lenton, A., and R. J. Matear (2007), Role of the Southern Annular Mode (SAM) in Southern Ocean CO₂ uptake, *Global Biogeochem. Cycles*, *21*, GB2016, doi:10.1029/2006GB002714.
- Lenton, A., et al. (2013), Sea-air CO₂ fluxes in the Southern Ocean for the period 1990–2009, *Biogeosciences*, *10*, 4037–4054, doi:10.5194/bg-10-4037-2013.
- Lewis, E., and D. W. R. Wallace (1998), *Program Developed for CO₂ System Calculations, ORNL/CDIAC-105*, Carbon Dioxide Information Analysis Center, Oak Ridge National Laboratory, U.S. Department of Energy, Oak Ridge, Tenn.
- Lovenduski, N. S., and N. Gruber (2008), Toward a mechanistic understanding of the decadal trends in the Southern Ocean carbon sink, *Global Biogeochem. Cycles*, *22*, GB3016, doi:10.1029/2007GB003139.
- Lovenduski, N. S., A. R. Fay, and G. A. McKinley (2015), Observing multi-decadal trends in Southern Ocean CO₂ uptake: What can we learn from an ocean model?, *Global Biogeochem. Cycles*, *29*, 416–426, doi:10.1002/2014GB004933.
- Marshall, G. J. (2003), Trends in the southern annular mode from observations and reanalyses, *J. Clim.*, *16*, 4134–4143.
- Matear, R. J., and A. C. Hirst (1999), Climate change feedback on the future oceanic CO₂ uptake, *Tellus B*, *51*, 722–733.
- McKinley, G. A., M. J. Follows, and J. Marshall (2004a), Mechanisms of air-sea CO₂ flux variability in the equatorial Pacific and the North Atlantic, *Global Biogeochem. Cycles*, *18*, GB2011, doi:10.1029/2003GB002179.
- McKinley, G. A., C. Rödenbeck, M. Gloor, S. Houweling, and M. Heimann (2004b), Pacific dominance to global air-sea CO₂ flux variability: A novel atmospheric inversion agrees with ocean models, *Geophys. Res. Lett.*, *31*, L22308, doi:10.1029/2004GL021069.
- McKinley, G. A., A. R. Fay, T. Takahashi, and N. Metzl (2011), Convergence of atmospheric and North Atlantic carbon dioxide trends on multidecadal timescales, *Nat. Geosci.*, *4*, 606–610, doi:10.1038/NGEO1193.
- McKinley, G. A., D. J. Pilcher, A. R. Fay, K. Lindsay, M. C. Long, and N. S. Lovenduski (2016), Timescales for detection of trends in the ocean carbon sink, *Nature*, *530*, 469–472, doi:10.1038/nature16958.
- Metzl, N., et al. (2010), Recent acceleration of the sea surface fCO₂ growth rate in the North Atlantic subpolar gyre (1993–2008) revealed by winter observations, *Global Biogeochem. Cycles*, *24*, GB4004, doi:10.1029/2009GB003658.
- Mikaloff Fletcher, S. E., et al. (2006), Inverse estimates of anthropogenic CO₂ uptake, transport, and storage by the ocean, *Global Biogeochem. Cycles*, *20*, GB2002, doi:10.1029/2005GB002530.
- Millero, F. J. (1995), Thermodynamics of the carbon dioxide system in the oceans, *Geochim. Cosmochim. Acta*, *59*, 661–677, doi:10.1016/0016-7037(94)00354-O.
- Müller, S. A., F. Joos, G.-K. Plattner, N. R. Edwards, and T. F. Stocker (2008), Modeled natural and excess radiocarbon: Sensitivities to the gas exchange formulation and ocean transport strength, *Global Biogeochem. Cycles*, *22*, GB3011, doi:10.1029/2007GB003065.
- Nightingale, P., G. Malin, C. Law, A. Watson, P. Liss, M. Liddicoat, J. Boutin, and R. Upstill-Goddard (2000), In situ evaluation of air-sea gas exchange parameterizations using novel conservative and volatile tracers, *Global Biogeochem. Cycles*, *14*(1), 373–387.
- Peylin, P., P. Bousquet, C. Le Quéré, S. Sitch, P. Friedlingstein, G. McKinley, N. Gruber, P. Rayner, and P. Ciais (2005), Multiple constraints on regional CO₂ flux variations over land and oceans, *Global Biogeochem. Cycles*, *19*, GB1011, doi:10.1029/2003GB002214.
- Peylin, P., et al. (2013), Global atmospheric carbon budget: Results from an ensemble of atmospheric CO₂ inversions, *Biogeosciences*, *10*, 6699–6720, doi:10.5194/bg-10-6699-2013.
- Pfeil, B., et al. (2013), A uniform, quality controlled Surface Ocean CO₂ Atlas (SOCAT), *Earth Syst. Sci. Data*, *5*, 125–143, doi:10.5194/essd-5-125-2013.
- Philander, S. G. (1990), *El Niño, La Niña, and the Southern Oscillation*, 293 pp., Academic Press, San Diego, Calif.
- Rayner, N. A., D. E. Parker, E. B. Horton, C. K. Folland, L. V. Alexander, D. P. Rowell, E. C. Kent, and A. Kaplan (2003), Global analyses of sea surface temperature, sea ice, and night marine air temperature since the late nineteenth century, *J. Geophys. Res.*, *108*(D14), 4407, doi:10.1029/2002JD002670.
- Rödenbeck, C., D. C. E. Bakker, N. Metzl, A. Olsen, C. Sabine, N. Cassar, F. Reum, R. F. Keeling, and M. Heimann (2014), Interannual sea-air CO₂ flux variability from an observation-driven ocean mixed-layer scheme, *Biogeosciences*, *11*(17), 4599–4613, doi:10.5194/bg-11-4599-2014.
- Rödenbeck, C., et al. (2015), Data-based estimates of the ocean carbon sink variability – First results of the Surface Ocean pCO₂ Mapping intercomparison (SOCOM), *Biogeosciences*, *12*, 7251–7278, doi:10.5194/bg-12-7251-2015.
- Sabine, C. L., et al. (2004), The oceanic sink for anthropogenic CO₂, *Science*, *305*(5682), 367–371, doi:10.1126/science.1097403.
- Sabine, C. L., et al. (2013), Surface Ocean CO₂ Atlas (SOCAT) gridded data products, *Earth Syst. Sci. Data*, *5*, 145–153, doi:10.5194/essd-5-145-2013.
- Sarmiento, J., and N. Gruber (2006), *Ocean Biogeochemical Dynamics*, 503 pp., Princeton Univ. Press, Princeton, N. J.
- Sarmiento, J. M., M. Gloor, N. Gruber, C. Beaulieu, A. R. Jacobson, S. E. Mikaloff Fletcher, S. Pacala, and K. Rodgers (2010), Trends and regional distributions of land and ocean carbon sinks, *Biogeosciences*, *7*, 2351–2367, doi:10.5194/bg-7-2351-2010.
- Sasse, T. P., B. I. McNeil, and G. Abramowitz (2013), A new constraint on global air-sea CO₂ fluxes using bottle carbon data, *Geophys. Res. Lett.*, *40*, 1594–1599, doi:10.1002/grl.50342.
- Schuster, U., and A. J. Watson (2007), A variable and decreasing sink for atmospheric CO₂ in the North Atlantic, *J. Geophys. Res.*, *112*, C11006, doi:10.1029/2006JC003941.
- Schuster, U., A. J. Watson, N. R. Bates, A. Corbière, M. González-Dávila, N. Metzl, D. Pierrot, and M. Santana-Casiano (2009), Trends in North Atlantic sea-surface fCO₂ from 1990 to 2006, *Deep-Sea Res. II*, *56*, 620–629.
- Schuster, U., et al. (2013), Atlantic and Arctic sea-air CO₂ fluxes, 1990–2009, *Biogeosciences*, *10*, 607–627, doi:10.5194/bg-10-607-2013.
- Steinman, B. A., M. E. Mann, and S. K. Miller (2015), Atlantic and Pacific multidecadal oscillations and Northern Hemisphere temperatures, *Science*, *347*, 988, doi:10.1126/science.1257856.
- Sweeney, C., E. Gloor, A. R. Jacobson, R. M. Key, G. McKinley, J. L. Sarmiento, and R. Wanninkhof (2007), Constraining global air-sea gas exchange for CO₂ with recent bomb ¹⁴C measurements, *Global Biogeochem. Cycles*, *21*, GB2015, doi:10.1029/2006GB002784.
- Takahashi, T., J. Olafson, J. Goddard, D. Chipman, and S. Sutherland (1993), Seasonal variations of CO₂ and nutrients in the high-latitude surface oceans: A comparative study, *Global Biogeochem. Cycles*, *7*(4), 843–878.
- Takahashi, T., et al. (2002), Global sea-air CO₂ flux based on climatological surface ocean pCO₂, and seasonal biological and temperature effects, *Deep-Sea Res. II*, *49*, 1601–1622.
- Takahashi, T., S. C. Sutherland, R. A. Feely, and C. E. Cosca (2003), *Decadal variation of the surface water pCO₂ in the western and eastern equatorial Pacific*, 852–856, vol. 302.
- Takahashi, T., et al. (2009), Climatological mean and decadal change in surface ocean pCO₂, and net sea-air CO₂ flux over the global oceans, *Deep-Sea Res. II*, *56*, 554–577.

- Takahashi, T., S. C. Sutherland, and A. Kozyr (2014), Global ocean surface water partial pressure of CO_2 database: Measurements performed during 1957–2012 (version 2013). ORNL/CDIAC-160, NDP-088(v2013), *Tech. Rep.*, Carbon Dioxide Information Analysis Center, Oak Ridge National Laboratory, U.S. Department of Energy, Oak Ridge, Tenn., doi:10.3334/CDIAC/OTG.NDP088(V2013).
- Thomas, H., F. A. E. Prowe, I. D. Lima, S. C. Doney, R. Wanninkhof, R. J. Greatbatch, U. Schuster, and C. A. (2008), Changes in the North Atlantic Oscillation influence CO_2 uptake in the North Atlantic over the past 2 decades, *Global Biogeochem. Cycles*, 22, GB4027, doi:10.1029/2007GB003167.
- Thompson, D. W. J., and J. M. Wallace (1998), The Arctic Oscillation signature in the wintertime geopotential height and temperature fields, *Geophys. Res. Lett.*, 25(9), 1297, doi:10.1029/98GL00950.
- Thompson, D. W. J., and J. M. Wallace (2000), Annular modes in the extratropical circulation. Part I: Month-to-month variability, *J. Clim.*, 13, 1000–1016, doi:10.1175/1520-0442(2000)013<1000:AMITEC>2.0.CO;2.
- Tjiputra, J., A. Olsen, K. Assmann, B. Pfeil, and C. Heinze (2012), A model study of the seasonal and long-term North Atlantic surface $p\text{CO}_2$ variability, *Biogeosciences*, 9(3), 907–923, doi:10.5194/bg-9-907-2012.
- Tjiputra, J., A. Olsen, L. Bopp, A. Lenton, B. Pfeil, T. Roy, J. Segsneider, I. Totterdell, and C. Heinze (2014), Long-term surface $p\text{CO}_2$ trends from observations and models, *Tellus. Series B*, 66, 23083, doi:10.3402/tellusb.v66.23083.
- Ullman, D. J., G. A. McKinley, V. Bennington, and S. Dutkiewicz (2009), Trends in the North Atlantic carbon sink: 1992–2006, *Global Biogeochem. Cycles*, 23, GB4011, doi:10.1029/2008GB003383.
- van Heuven, S., D. Pierrot, J. W. B. Rae, E. Lewis, and D. W. R. Wallace (2011), *Matlab Program Developed for CO_2 System Calculations. ORNL/CDIAC-105b*, Carbon Dioxide Information Analysis Center, Oak Ridge National Laboratory, U.S. Department of Energy, Oak Ridge, Tenn.
- Wanninkhof, R. (1992), Relation between wind speed and gas exchange over the ocean, *J. Geophys. Res.*, 97, 7373–7383.
- Wanninkhof, R., and W. McGillis (1999), A cubic relationship between air-sea CO_2 exchange and wind speed, *Geophys. Res. Lett.*, 26(13), 1889–1892.
- Wanninkhof, R., et al. (2013), Global ocean carbon uptake: Magnitude, variability and trends, *Biogeosciences*, 10, 1983–2000, doi:10.5194/bg-10-1983-2013.
- Watson, A. J., et al. (2009), Tracking the variable North Atlantic sink for atmospheric CO_2 , *Science*, 326(5958), 1391–1393, doi:10.1126/science.1177394.
- Weiss, R. F. (1974), Carbon dioxide in water and seawater: The solubility of a non-ideal gas, *Mar. Chem.*, 2, 203–215.
- Wolter, K., and M. S. Timlin (2011), El Niño/Southern Oscillation behaviour since 1871 as diagnosed in an extended multivariate ENSO index (MEI.ext), *Intl. J. Climatol.*, 31, 1074–1087.
- Zeng, J., Y. Nojiri, P. Landschützer, M. Telszewski, and S. Nakaoka (2014), A global surface ocean fCO_2 climatology based on a feed-forward neural network, *J. Atmos. Oceanic Technol.*, 31, 1838–1849, doi:10.1175/JTECH-D-13-00137.1.
- Zhang, Y., J. M. Wallace, and D. S. Battisti (1997), ENSO-like interdecadal variability: 1900–93, *J. Clim.*, 10, 1004–1020.